

Multicompartment Magnetic Resonance Fingerprinting

Sunli Tang^{*1}, Carlos Fernandez-Granda^{*1,2}, Sylvain Lannuzel^{2,3}, Brett Bernstein¹, Riccardo Lattanzi^{4,5}, Martijn Cloos^{4,5}, Florian Knoll^{4,5}, and Jakob Assländer^{4,5}

¹Courant Institute of Mathematical Sciences, New York University

²Center for Data Science, New York University

³École CentraleSupélec

⁴Center for Biomedical Imaging, Department of Radiology, New York University School of Medicine

⁵Center for Advanced Imaging and Innovation Research (CAI²R), Department of Radiology, New York University School of Medicine

February 2018

Abstract

Magnetic resonance fingerprinting (MRF) is a technique for quantitative estimation of spin-relaxation parameters from magnetic-resonance data. Most current MRF approaches assume that only one tissue is present in each voxel, which neglects the tissue’s microstructure, and may lead to artifacts in the recovered parameter maps at boundaries between tissues. In this work, we propose a multicompartment MRF model that accounts for the presence of multiple tissues per voxel. The model is fit to the data by iteratively solving a sparse linear inverse problem at each voxel, in order to express the magnetization signal as a linear combination of a few fingerprints in the precomputed dictionary. Thresholding-based methods commonly used for sparse recovery and compressed sensing do not perform well in this setting due to the high local coherence of the dictionary. Instead, we solve this challenging sparse-recovery problem by applying reweighted- ℓ_1 -norm regularization, implemented using an efficient interior-point method. The proposed approach is validated with simulated data at different noise levels and undersampling factors, as well as with a controlled phantom imaging experiment on a clinical magnetic-resonance system.

Keywords. Quantitative MRI, magnetic resonance fingerprinting, multicompartment models, parameter estimation, sparse recovery, coherent dictionaries, reweighted ℓ_1 -norm.

*Sunli Tang and Carlos Fernandez-Granda contributed equally to this paper.

1 Introduction

1.1 Quantitative magnetic resonance imaging

Magnetic resonance imaging (MRI) is a medical-imaging technique that measures the response of the atomic nuclei in biological tissues to high-frequency radio waves when placed in a strong magnetic field [45]. Due to its superior soft-tissue contrast, MRI has become a key technology for non-invasive diagnostics. In contrast to other medical imaging modalities such as computed tomography or positron emission tomography, MR images are usually qualitative in nature. They consist of gray values that capture relative signal intensity changes between certain tissues, which are then interpreted by radiologists to detect pathologies.

Due to their qualitative nature, MR images are subject to variations between different MRI systems and particular data-acquisition settings, hampering reproducibility. This makes it very challenging to use data from current clinical MRI systems for longitudinal studies, early detection and progress-tracking of disease, as well as computer-aided diagnosis. The goal of quantitative MRI is to measure physical parameters *quantitatively*, in a way that is reproducible across different MRI systems [23, 34, 67, 69]. Some of these quantities, such as spin-relaxation times, have great potential as quantitative biomarkers for various pathologies [53, 56, 63] and allow to synthesize images with standardized image contrasts [26, 59]. Unfortunately, data-acquisition protocols for quantitative MRI often lead to long measurement times that are challenging to integrate in the clinical workflow and as a consequence are not widely deployed.

1.2 Magnetic resonance fingerprinting

Magnetic resonance fingerprinting (MRF) [48] is a recent approach to quantitative MRI designed to measure tissue-relaxation parameters within clinically-feasible scan times. MRF departs from traditional MRI acquisition by deliberately avoiding a steady state of the magnetization. For a fixed value of the parameters of interest, the signal evolution of the magnetization at a given voxel (which results from the train of radiofrequency pulses and gradient waveforms used to acquire the data) can be simulated by solving a system of differential equations, called the Bloch Equations [9]. This makes it possible to precompute a dictionary of possible signals or *fingerprints* associated with different values of the relaxation parameters. An estimate of the actual values consistent with the data can then be obtained by finding the fingerprint that best matches the observed measurements. This approach has been shown to be robust to technical imperfections of the scanner hardware, such as inhomogeneities of the magnetic fields used to generate the MR signal [21].

Current MRF methods usually assume that only one type of tissue with a well-defined set of relaxation times is present in each voxel, which degrades their accuracy when this *single-compartment* assumption is violated. Fitting a single-compartment model to data obtained from a voxel with several tissues yields erroneous parameter estimates that may not correspond to any of the contributing compartments, as illustrated in Figure 1. As a result of this *partial-volume* effect [70], single-compartment MRF methods do not accurately characterize boundaries between tissues, as discussed by the original developers of MRF [26]. This limitation is particularly problematic in applications that require geometric measurements, such as the diagnostic of Alzheimers disease, where cortical thickness provides a promising biomarker for early detection [39].

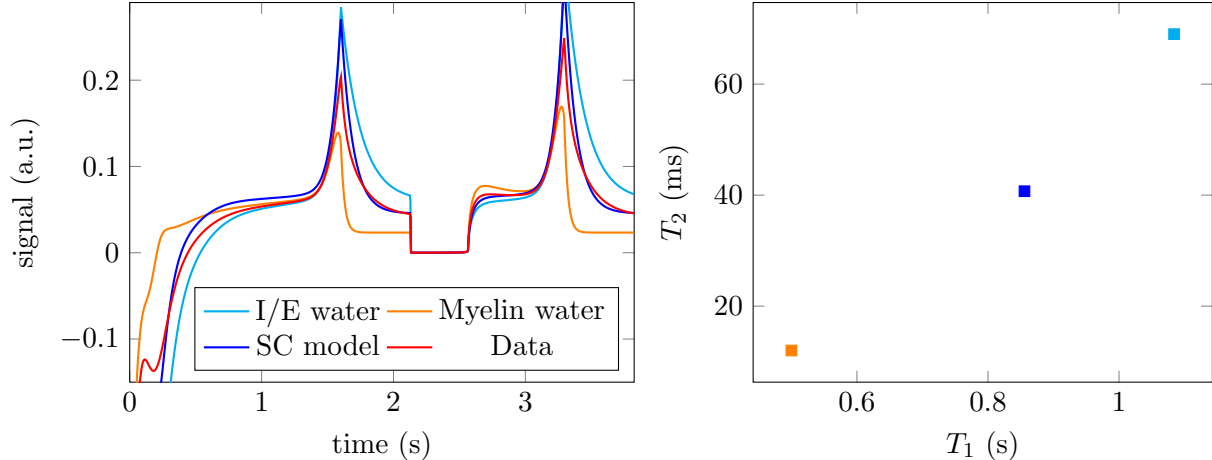


Figure 1: The left image shows the simulated signals corresponding to two different tissues: intra/extra (I/E) axonal water (light blue) and myelin water (orange). The signal in a voxel containing both tissues corresponds to the sum of both signals (red). A single-compartment (SC) model (blue) is not able to approximate the data (left) and results in an inaccurate estimate of the relaxation parameters T_1 and T_2 even in the absence of noise (right). The MRF dictionary is generated using the approach described in [3].

Single-compartment models also fail to account for other intra-voxel structure. Due to the limited spatial resolution of MRI (on the order of a millimeter), the cellular microstructure of biological tissues results in multiple-tissue compartments being present even in voxels that are not necessarily at tissue boundaries. An important example is white matter in the brain, which consists of signal contributions of extra- and intra-axonal water with similar relaxation times, as well as water trapped between the myelin sheets, with substantially shorter relaxation times [43] (Figure 1 is based on this example). If a particular disease causes demyelination, this leads to a corresponding reduction of one of these compartments (the so-called myelin-water fraction) [44]. Multicompartment models make it possible to evaluate the myelin-water fraction within a voxel, which is therefore useful for the diagnosis of neurodegenerative diseases such as multiple sclerosis [43, 44].

It is important to note that the cellular structure of biological tissue generally does not result in entirely separated compartments within each voxel. In fact, one can observe chemical exchange of water molecules between compartments [1]. However, in the case of tissue boundaries, these effects play a subordinate role due to the macroscopic nature of the interfaces. Similarly, in the case of myelin-water imaging, neglecting chemical exchange is a reasonable and commonly-used assumption in the literature [44]. In this work, we consider a multicompartment model that incorporates this assumption. As a result, the measured signal at a given voxel corresponds to the sum of the signals corresponding to the individual tissues present in the voxel [54].

1.3 Related work

Previous works applying multicompartment estimation in the context of myelin-water imaging, applied bi-exponential fitting to data obtained from a multi-echo experiment [43, 44]. Other works used

non-convex optimization to fit a multicompartment model to measurements from a multi-steady-state experiment [24, 25]. In the context of MR fingerprinting, the multicompartment problem has been tackled by exhaustive search in [38]. The work that lies closer to our proposed approach is [54], which applies a reweighted-least-squares method based on a Bayesian framework to fit the multicompartment parameters to MRF data. This method produces a dense solution for each compartment in the parameter space, which must then be post-processed to produce the parameter estimates. In contrast, our proposed method yields sparse solutions, from which the parameters can usually be estimated directly.

Sparse linear models are a fundamental tool in statistics [32, 40], signal processing [51] and machine learning [49], as well as across many applied domains [47, 76]. Most works that apply these models to recover sparse signals focus on incoherent measurements [8, 14, 17, 27, 28, 36, 55, 71]. As explained in more detail in Section 2.4, this setting is not relevant to MRF where dictionary columns can be highly correlated. Instead, the present work is more related to recent advances in optimization-based methods for sparse recovery from coherent dictionaries [7, 15, 29, 30, 50]. Related applied work includes the application of these techniques to source localization in electroencephalography [65, 78], analysis of positron-emission tomography data [37, 41] and radar imaging [61]. In addition, our work combines insights from recovery methods based on reweighting convex sparsity-inducing norms [19, 74] and techniques for distributed optimization [11].

1.4 Contributions

The main contribution of this work is a method for fitting multicompartment MRF models. These models explain the signal evolution of a voxel using a small number of precomputed basis functions or *fingerprints*, which requires solving a sparse linear inverse problem. We combine the following insights to solve this challenging inverse problem both accurately and efficiently:

- Fitting the multicompartment model can be decoupled into multiple sparse-recovery problems—one for each voxel—using the alternating-direction of multipliers framework (see Section 2.2).
- The correlations between atoms in the dictionary make it possible to compress the dictionary to decrease the computational cost (see Section 2.3).
- Thresholding-based algorithms, typically used for sparse recovery and compressed sensing, do not perform well on the multicompartment MRF problem, due to the high correlation between dictionary atoms. However, ℓ_1 -norm minimization does succeed in achieving exact recovery in the absence of noise as long as the problem is solved using higher-precision second-order methods (see Section 2.4).
- The sparse-recovery approach can be made robust to noise and model imprecisions by using reweighted- ℓ_1 -norm methods (see Section 2.5).
- These reweighted methods can be efficiently implemented using a second-order interior-point solver described in Section 2.6.

We validate our proposed method via numerical experiments on simulated data (Section 3.1), as well as on experimental data from a custom-built phantom using a clinical MR system (see Section 3.2).

2 Methods

2.1 Multicompartment model

In this work, we consider the problem of estimating the relaxation times T_1 and T_2 from magnetic-resonance data. T_1 is the time constant that governs the relaxation of the components of the nuclear-spin magnetization vector that are parallel to the external magnetic field. T_2 relaxation affects the components that are perpendicular to the external field [57].

Magnetic-resonance fingerprinting (MRF) [48] is based on the following insight. For a fixed data-acquisition scheme, the mapping between the time-relaxation parameters T_1 and T_2 of a particular tissue and the corresponding magnetization signal measured by the MRI system is not known explicitly, but it can be *simulated numerically* by solving a system of differential equations, called the Bloch Equations [9]. This makes it possible to construct a dictionary of possible signal evolutions or *fingerprints*, each corresponding to a specific value of the relaxation times.

Let us denote the signal measured at a voxel j by the vector

$$x^{[j]} := \begin{bmatrix} x_{t_1}^{[j]} \\ x_{t_2}^{[j]} \\ \dots \\ x_{t_n}^{[j]} \end{bmatrix}, \quad (2.1)$$

where t_1, t_2, \dots, t_n are the times at which the signal is sampled. We assume that the signal is well described as an additive superposition of fingerprints in the precomputed dictionary $D \in \mathbb{R}^{n \times m}$ (there are m possible fingerprints),

$$x^{[j]} = Dc^{[j]}, \quad 1 \leq j \leq N, \quad (2.2)$$

where N is the number of voxels in the volume of interest. The vectors of coefficients $c^{[1]}, c^{[2]}, \dots, c^{[N]}$ are assumed to be sparse and nonnegative: each nonzero entry in $c^{[j]}$ corresponds to the proton density of a tissue that is present in voxel j .

Raw MRI data sampled at a given time do not directly correspond to the magnetization signal of the different voxels, but rather to samples from the spatial Fourier transform of the magnetization over all voxels in the volume of interest [46], a representation known as *k-space* in the MRI literature [72]. Staying within clinically-feasible scan times in MRF requires subsampling the image k-space and therefore violating the Nyquist-Shannon sampling theorem [48]. The k-space is typically subsampled along different trajectories, governed by changes in the magnetic-field gradients used in the measurement process. We define a linear operator $F_{t_i} \in \mathbb{C}^{d \times n}$ that represents the linear operator mapping the magnetization at time t_i to the measured data $y_{[t_i]} \in \mathbb{C}^d$, where d is the number of k-space samples at t_i . This operator encodes the chosen subsampling pattern in the

frequency domain. The model for the data is consequently of the form

$$y_{t_i} = F_{t_i} \begin{bmatrix} x_{t_i}^{[1]} \\ x_{t_i}^{[2]} \\ \vdots \\ x_{t_i}^{[N]} \end{bmatrix}, \quad 1 \leq i \leq n, \quad (2.3)$$

where we have ignored noise and model inaccuracies. If the data are acquired using multiple receive coils, the measurements can be modeled as samples from the spectrum of the pointwise product between the magnetization and the sensitivity function of the different coils [62, 66]. In that case the operator F_{t_i} also includes the sensitivity functions and d is the number of k-space samples multiplied by the number of coils.

2.2 Parameter Map Reconstruction via Alternating Minimization

For ease of notation, we define the magnetization and coefficient matrices

$$X := [x^{[1]}, x^{[2]}, \dots, x^{[N]}], \quad (2.4)$$

$$C := [c^{[1]}, c^{[2]}, \dots, c^{[N]}], \quad (2.5)$$

so that we can write (2.2) as

$$X = DC. \quad (2.6)$$

In addition we define the data matrix $Y \in \mathbb{C}^{d \times n}$

$$Y := [y_{t_1}, y_{t_2}, \dots, y_{t_n}] \quad (2.7)$$

and a linear operator \mathcal{F} such that

$$Y = \mathcal{F}X. \quad (2.8)$$

Note that by (2.3) the i th column of Y is the result of applying F_{t_i} to the i th row of X .

In principle, we could fit the coefficient matrix by computing a sparse estimate such that $Y \approx \mathcal{F}DC$. Unfortunately, this would require solving a sparse-regression problem of intractable dimensions. Instead we incorporate a variable \tilde{X} to represent the magnetization and formulate the model-fitting problem as

$$\underset{\tilde{X}, \tilde{C}}{\text{minimize}} \quad \left\| Y - \mathcal{F}\tilde{X} \right\|_F^2 \quad (2.9)$$

$$\text{subject to} \quad \tilde{X} = D\tilde{C}, \quad (2.10)$$

with the additional constraint that the entries of \tilde{C} are sparse and nonnegative. In order to alternate between updating the magnetization and coefficient variables, we follow the framework of

the alternative-direction method of multipliers (ADMM) [11]. Consider the augmented Lagrangian with respect to the constraint (2.10),

$$\mathcal{L}_\mu(\tilde{X}, \tilde{C}, \Lambda) := \left\| Y - \mathcal{F}\tilde{X} \right\|_F^2 + \langle \Lambda, \tilde{X} - D\tilde{C} \rangle + \frac{\mu}{2} \left\| \tilde{X} - D\tilde{C} \right\|_F^2, \quad (2.11)$$

where the constant $\mu > 0$ is a parameter and the dual variable Λ is an $N \times n$ matrix. ADMM alternates between minimizing the augmented Lagrangian with respect to each primal variable sequentially and updating the dual variable. We now describe each of the updates in more detail. We denote the values of the different variables at iteration l by $C^{(l)}$, $X^{(l)}$ and $\Lambda^{(l)}$. More details on the implementation can be found in Ref. [2].

Updating \tilde{X}

If we fix \tilde{C} and Λ , minimizing \mathcal{L}_μ over \tilde{X} is equivalent to solving the least-squares problem

$$X^{(l+1)} := \arg \min_{\tilde{X}} \left\| Y - F\tilde{X} \right\|_F^2 + \frac{\mu}{2} \left\| \tilde{X} - DC^{(l)} - \frac{1}{\mu}\Lambda^{(l)} \right\|_F^2. \quad (2.12)$$

This step amounts to estimating a magnetization matrix that fits the data while being close to the magnetization corresponding to the current estimate of dictionary coefficients. The optimization problem has a closed-form solution, but due to the size of the matrices it is more efficient to solve it using an iterative algorithm such as the conjugate-gradients method [64].

Updating \tilde{C}

If we fix \tilde{X} and Λ , minimizing \mathcal{L}_μ over \tilde{C} decouples into N subproblems. In more detail, the goal is to compute a sparse nonnegative vector of coefficients $\tilde{c}^{[j]}$ for each voxel j , $1 \leq j \leq N$, such that

$$\left(X^{(l)} - \frac{1}{\mu}\Lambda^{(l)} \right)_j \approx D \tilde{c}^{[j]}, \quad (2.13)$$

where the left hand side corresponds to the j th column of $X^{(l)} - \frac{1}{\mu}\Lambda^{(l)}$. This collection of sparse-recovery problems is very challenging to solve due to the correlations between the columns of D . In Sections 2.4, 2.5 and 2.6 we present an algorithm to tackle them efficiently.

Updating Λ

The dual variable is updated by setting

$$\Lambda^{(l+1)} := \Lambda^{(l)} + \mu \left(X^{(l)} - \hat{D}C^{(l)} \right). \quad (2.14)$$

We refer to [11] for a justification based on dual-ascent methods.

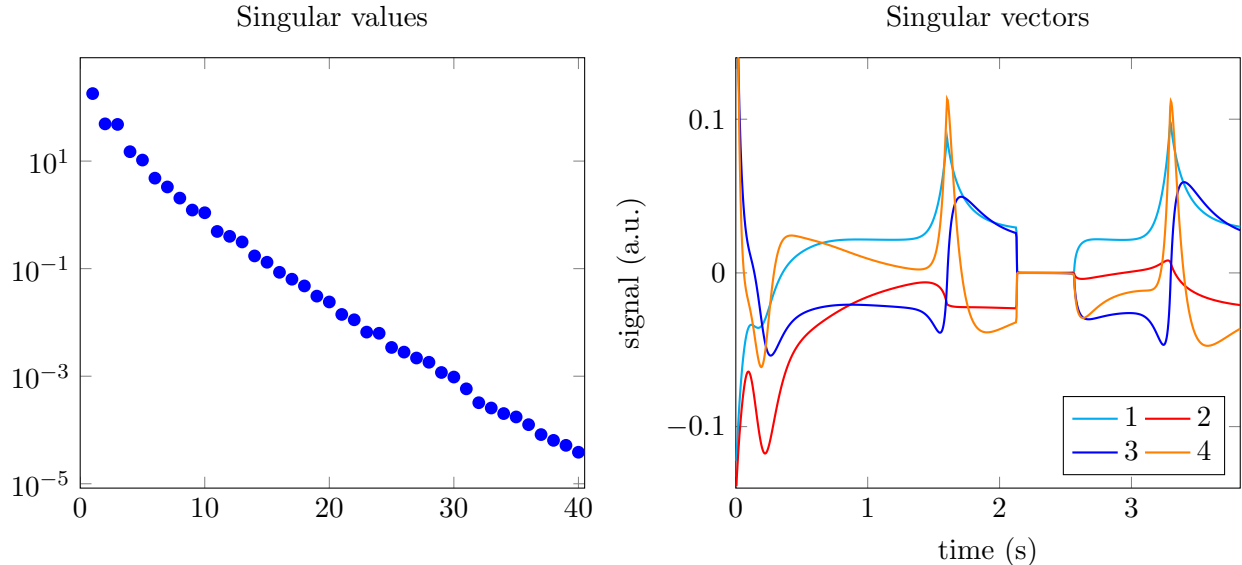


Figure 2: Singular values (left) and corresponding left singular vectors (right) of an MRF dictionary generated using the approach in [3,4].

2.3 Dictionary compression

As explained in Section 2.4 the columns in the dictionary of fingerprints D are highly correlated. Consequently, D is approximately low rank: if we consider its singular value decomposition

$$D = U\Sigma V^T, \quad (2.15)$$

where the superscript T denotes the transpose. The singular values in Σ present a rapid decay, so its column space is well approximated as the span of the first few left singular vectors (see Figure 2). Following [2,54], we exploit this low-rank structure to compress the dictionary. Let $U_k\Sigma_k V_k^T$ denote the rank- k truncated SVD of D , where U_k contains the first k left singular vectors and Σ_k and V_k the corresponding singular values and right singular vectors. If the measured data follow the linear model $Y \approx \mathcal{F}DC$, then

$$Y \approx \mathcal{F}U_k\Sigma_k V_k^T C \quad (2.16)$$

$$= \bar{\mathcal{F}}\bar{D}C, \quad (2.17)$$

where $\bar{\mathcal{F}} := \mathcal{F}U_k$ is a modified linear operator and

$$\bar{D} := \Sigma_k V_k^T \quad (2.18)$$

$$= U_k^T D. \quad (2.19)$$

\bar{D} can be interpreted as a compressed dictionary with dimensions $k \times m$ obtained by projecting each fingerprint onto the k -dimensional subspace spanned by the columns of U_k , which are depicted on the right image of Figure 2. In our experiments, D is well approximated by $U_k\Sigma_k V_k^T$ for values of k between 10 and 15. As a result, replacing \mathcal{F} by $\bar{\mathcal{F}}$ and D by \bar{D} within the ADMM framework in Section 2.2 dramatically decreases the computational cost.

2.4 Sparse estimation via ℓ_1 -norm minimization

In this section, we consider the problem of estimating the tissue parameters at a fixed voxel from the time evolution of its magnetization signal. As described in Section 2.2, this is a crucial step in fitting the MRF multicompartment model. To simplify the notation, we denote the discretized magnetization signal at an arbitrary voxel by $x \in \mathbb{R}^n$ (where n is the number of time samples) and the sparse vector of coefficients by $c \in \mathbb{R}^m$. In Eq. (2.13), x represents the column of $X^{(l)} - \frac{1}{\mu}\Lambda^{(l)}$ corresponding to the voxel at a particular iteration l of the alternating scheme.

Let us first consider the sparse recovery problem assuming that the magnetization estimate is exact. In that case there exists a sparse vector c such that

$$x = Dc. \tag{2.20}$$

Even in this simplified scenario, computing c from x is very challenging. The dictionary is overcomplete: there are more columns than time samples because the number of fingerprints m is larger than the number of time samples n . As a result the linear system is underdetermined: there are infinite possible solutions. However, we are not interested in arbitrary solutions, but rather in sparse solutions, where c contains a small number of nonzero entries corresponding to the tissues present in the voxel.

There is a vast literature on the recovery of sparse signals from underdetermined linear measurements. Two popular techniques are greedy methods that select columns from the dictionary sequentially [52, 60] and optimization-based approaches that minimize a sparsity-promoting cost function such as the ℓ_1 norm [16, 20, 27]. Theoretical analysis of these methods has established that they achieve exact recovery and are robust to additive noise if the overcomplete dictionary is *incoherent*, meaning that the correlation between the columns in the dictionary is low [8, 14, 17, 27, 28, 36, 55, 71]. Some of these works assume stronger notions of incoherence such as the restricted-isometry condition [17] or the restricted-eigenvalue condition [8].

Unfortunately, MRF dictionaries are highly coherent: the correlation between fingerprints corresponding to similar parameters is very high. This is illustrated by Figure 3, which shows the correlations between columns for a simple MRF dictionary simulated following [3, 4]. For ease of visualization, the only parameter that varies in the dictionary is T_1 (the value of T_2 is fixed to 62 ms), so that the correlation in the depicted dictionary has a very simple structure: neighboring columns correspond to similar values of T_1 and are, therefore, more correlated, whereas well-separated columns are less correlated. For comparison, the figure also shows the correlations between columns for a typical incoherent compressed-sensing dictionary generated by sampling each entry independently from a Gaussian distribution [18, 27].

Coherence is not only a problem from a theoretical point of view. Most fast-estimation methods for sparse recovery exploit the fact that for incoherent dictionaries like the Gaussian dictionary in Figure 3 the Gram matrix $D^T D$ is close to the identity. As a result, multiplying the data by the transpose of the dictionary yields a noisy approximation to the sparse coefficients

$$D^T y = D^T Dc \approx c, \tag{2.21}$$

which can be *cleaned up* using some form of thresholding. This concept is utilized by greedy approaches such as orthogonal matching pursuit [60] or iterative hard-thresholding methods [10],

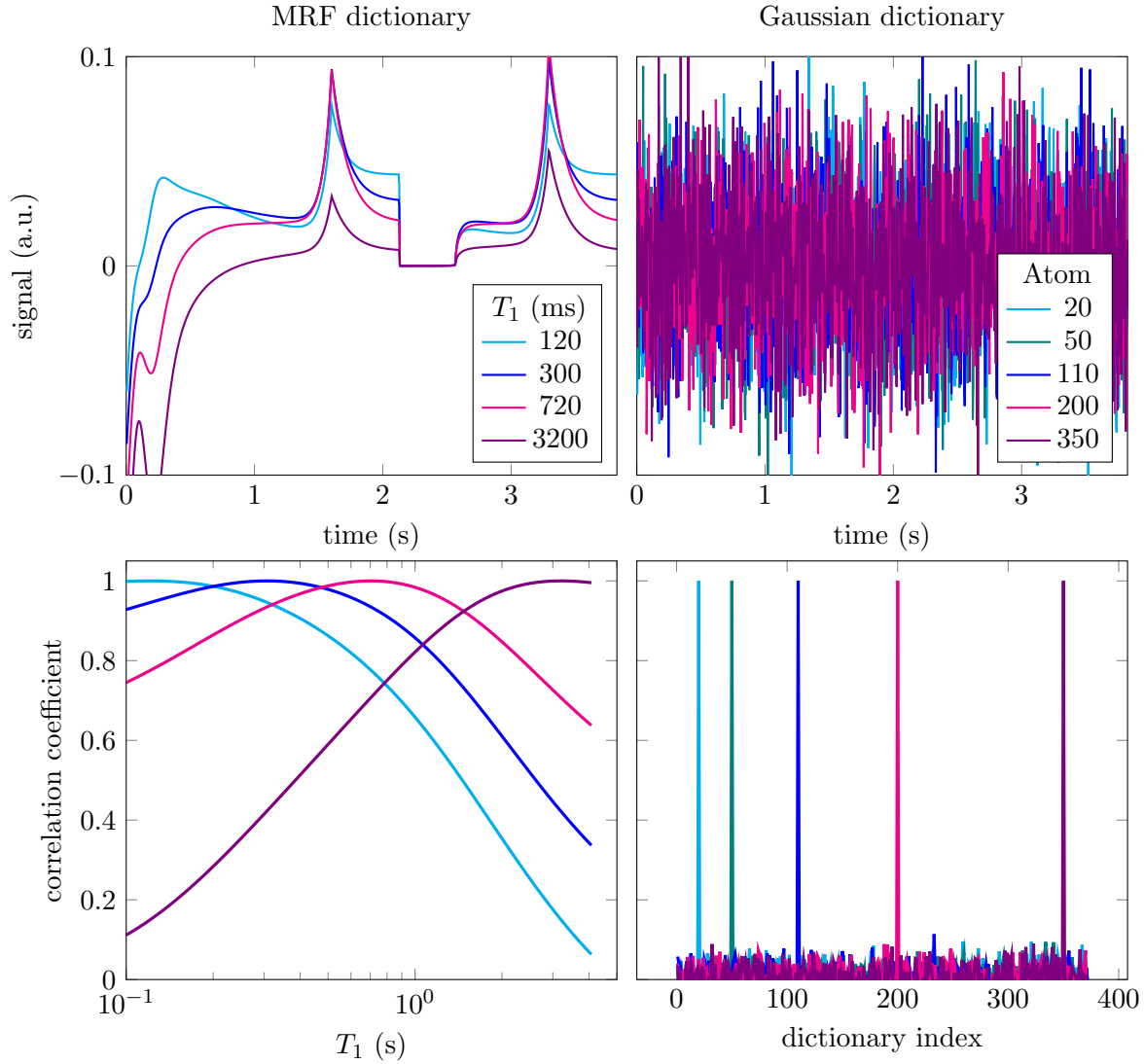


Figure 3: The figure shows a small selection of columns in a magnetic-resonance fingerprinting (MRF) dictionary (top left) and an i.i.d. Gaussian compressed-sensing dictionary (top right). In the MRF dictionary, generated using the approach in [3, 4], each column corresponds to the time evolution of the magnetization for a value of the relaxation parameter T_1 (for simplicity T_2 is fixed to 62 ms). In the bottom row we show the correlation of the selected columns with every other column in the dictionary. This reveals the high local coherence of the MRF dictionary (left), compared to the incoherence of the compressed-sensing dictionary (right).

as well as fast algorithms for ℓ_1 -norm minimization such as proximal methods [22] and coordinate descent [33], which use iterative soft-thresholding instead. When the dictionary is coherent, and $D^T y$ is no longer approximately sparse, these techniques are extremely slow and often fail to converge to a sparse estimate. As an example Figure 4 shows the result of applying the fast iterative shrinkage-thresholding algorithm (FISTA) [5] to an MRF dictionary. The estimated coefficients are not sparse, which is consistent with numerical experiments reported in other works [54].

Recently, theoretical guarantees for sparse-decomposition methods have been established for dictionaries arising in super-resolution [15, 30] and deconvolution problems [7]. As in the case of MRF, these dictionaries have very high local correlations between columns. These papers show that although robust recovery of all sparse signals in such dictionaries is not possible due to their high coherence, ℓ_1 -norm minimization achieves exact recovery of a more restricted class of signals: sparse superpositions of dictionary columns that are not highly correlated. To be clear, there may be arbitrarily high local correlations in the dictionary, as long the columns that are actually present in the measured signal are relatively uncorrelated with each other. In the case of MRF, this corresponds to a multicompartment model where the fingerprints of the tissues present in each voxel are sufficiently different. Our numerical results indicate that solving the convex program

$$\underset{\tilde{c} \in \mathbb{R}^m}{\text{minimize}} \quad \|\tilde{c}\|_1 \tag{2.22}$$

$$\text{subject to} \quad D\tilde{c} = x \tag{2.23}$$

$$\tilde{c} \geq 0. \tag{2.24}$$

makes it possible to successfully fit the sparse multicompartment model, as long as the parameters of each compartment are not too close (see Figure 8). Crucially, we observe that it is necessary to use high-precision second-order methods [35] in order to achieve exact recovery. In contrast, fast ℓ_1 -norm minimization algorithms based on soft-thresholding or coordinate descent converge extremely slowly or fail to achieve exact recovery due to the coherence of the dictionary, as illustrated by the example in Figure 4. The nonnegative constraint in (2.24) stems from the fact that the coefficients in the multicompartment model correspond to the proton densities of each tissue and, therefore, cannot be negative. In practice, this constraint implies that all compartments have the same complex phase.

2.5 Robust sparse estimation via reweighted- ℓ_1 -norm minimization

In the previous section, we discuss exact recovery of the sparse coefficients in a multicompartment model under the assumptions that (1) there is no noise and (2) the fingerprints corresponding to the true parameters are present in the dictionary. In practice, neither of these assumptions holds: noise is unavoidable, the tissue parameters may have any value in the continuous parameter space and the data x used to fit the model is perturbed by aliasing artifacts (recall that it corresponds to a column in $X^{(l)} - \frac{1}{\mu}\Lambda^{(l)}$ at iteration l of the alternating scheme described in Section 2.2). A standard way to account for additive noise and model imprecisions in sparse-recovery problems is to relax the ℓ_1 -norm minimization problem (2.24) to a regularized least-squares problem of the form

$$\begin{aligned} \underset{\tilde{c} \in \mathbb{R}^m}{\text{minimize}} \quad & \frac{1}{2} \|D\tilde{c} - x\|^2 + \lambda \|\tilde{c}\|_1 \\ \text{subject to} \quad & \tilde{c} \geq 0 \end{aligned} \tag{2.25}$$

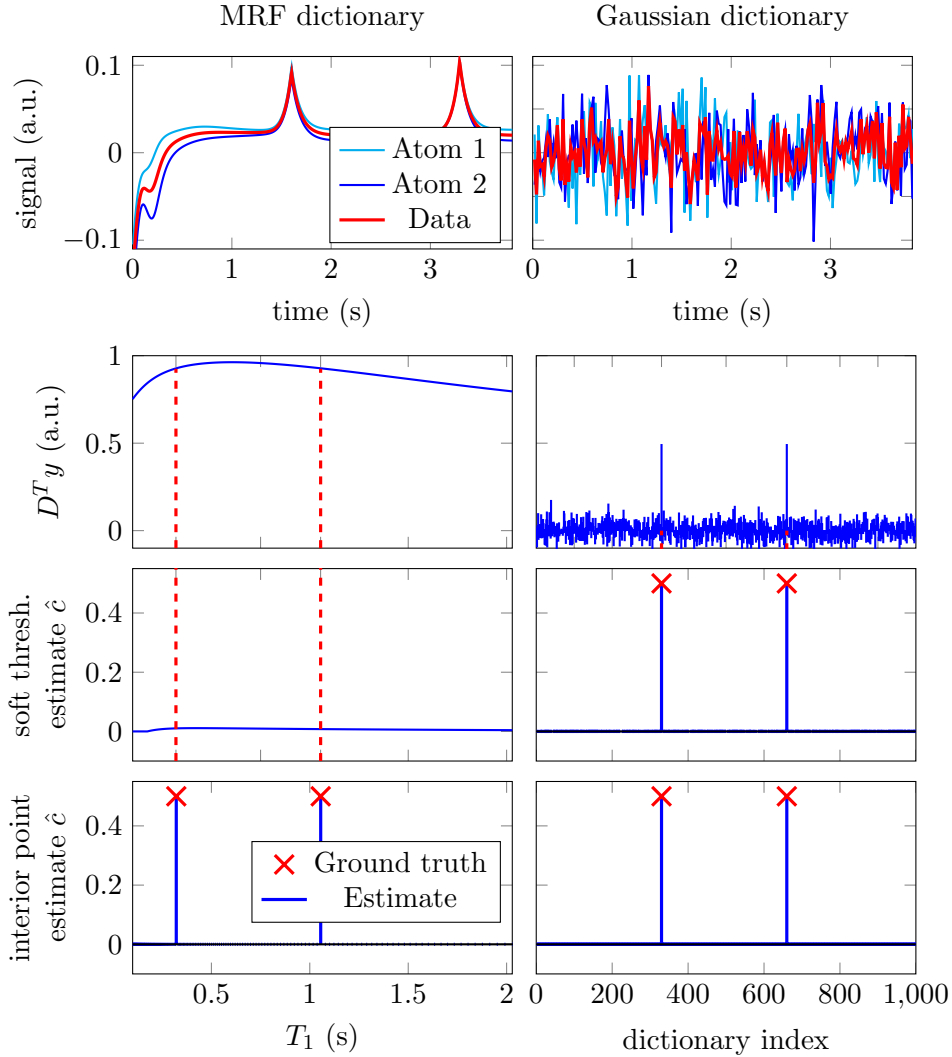


Figure 4: The data in the top row are an additive superposition of two columns from the MRF (left) and the compressed-sensing (right) dictionaries depicted in Figure 3. The correlation between the data and each dictionary column (second row) is much more informative for the incoherent dictionary (right) than for the coherent one (left). A fast first-order method [5, 6] designed to solve problem (2.24) (third row) achieves exact recovery of the true support for the compressed-sensing problem (right), but fails for MRF (left). In contrast, solving (2.24) using a high-precision solver [35] achieves exact recovery in both cases (bottom row).

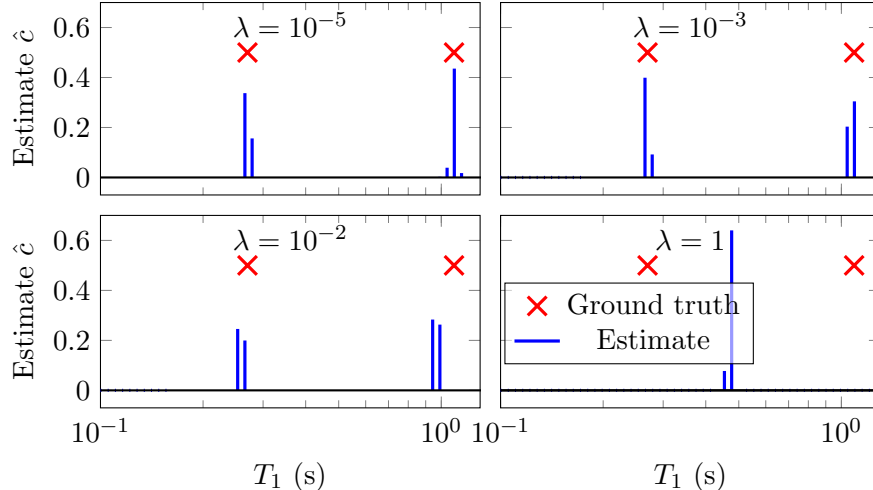


Figure 5: Estimates for the components of an MRF signal obtained by solving problem (2.25) for different values of the parameter λ using a high-precision solver [35]. The data are generated by adding i.i.d. Gaussian noise to the two-compartment MRF signal shown in Figure 4 (top left). The signal-to-noise ratio (defined as the ratio between the ℓ_2 norm of the signal and the noise) is equal to 100.

where $\lambda \geq 0$ is a regularization parameter that governs the trade-off between the least-squares data-consistency term and the ℓ_1 -norm regularization term. Solving (2.25) to perform sparse recovery is a popular sparse-regression method known as the lasso in statistics [68] and basis pursuit in signal processing [20].

Figure 5 shows the results of estimating the components of a noisy MRF signal by solving problem (2.25) for different values of the parameter λ . For large values of λ , the solution is sparse, but the fit to the data is not very accurate and the true support is not well approximated. For small values of λ , the solution to the convex program correctly locates the vicinity of the true coefficients, but it is contaminated by small spurious spikes. Reweighted- ℓ_1 -methods [19, 74] are designed to enhance the performance of ℓ_1 -norm-regularized problems by promoting sparser solutions that are close to the initial estimate. In the case of the MRF dictionary, these methods are able to remove the spurious small spikes while retaining an accurate support estimate. This is achieved by solving a sequence of weighted ℓ_1 -norm regularized problems of the form

$$\begin{aligned} & \underset{\tilde{c} \in \mathbb{R}^m}{\text{minimize}} && \frac{1}{2} \|D\tilde{c} - x\|^2 + \lambda \sum_{i=1}^m \omega_i^{(k)} \tilde{c}_i \\ & \text{subject to} && \tilde{c} \geq 0 \end{aligned} \quad (2.26)$$

for $k = 1, 2, \dots$. We denote the solution of this optimization problem by $\hat{c}^{(k)}$. The entries in the initial vector of weights $\omega^{(1)}$ are initialized to one, so $\hat{c}^{(1)}$ is the solution to problem (2.25). The weights are then updated depending on the subsequent solutions to problem (2.26).

We consider two different reweighting schemes. The first, proposed in [19], simply sets the weights

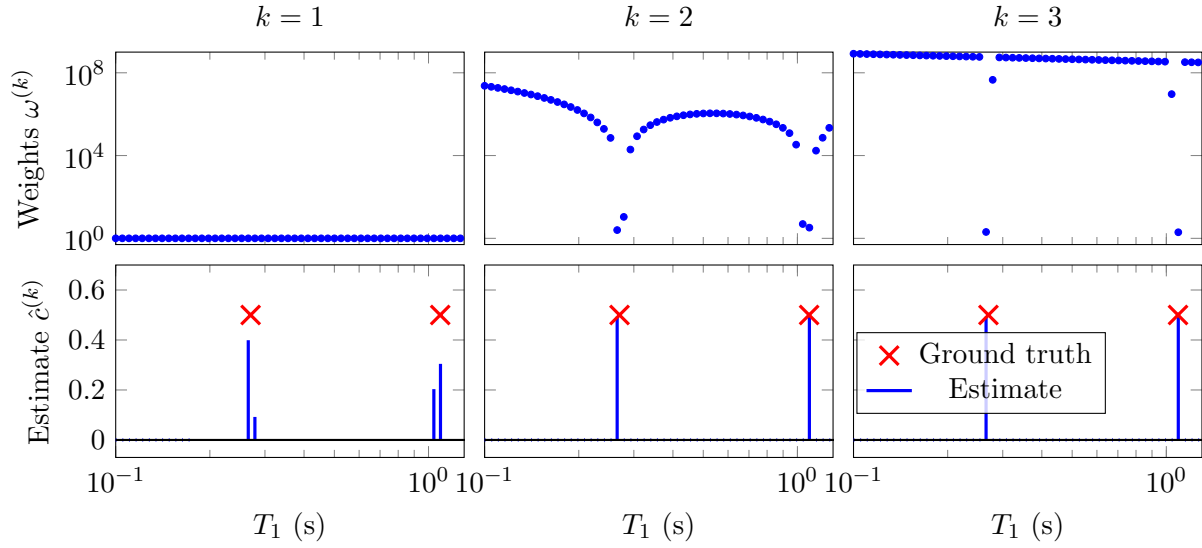


Figure 6: Solutions to problem (2.26) (bottom) and corresponding weights (top) computed following the reweighting scheme (2.27), with $\lambda := 10^{-3}$ and $\epsilon := 10^{-8}$. The data are the same as in Figure 5.

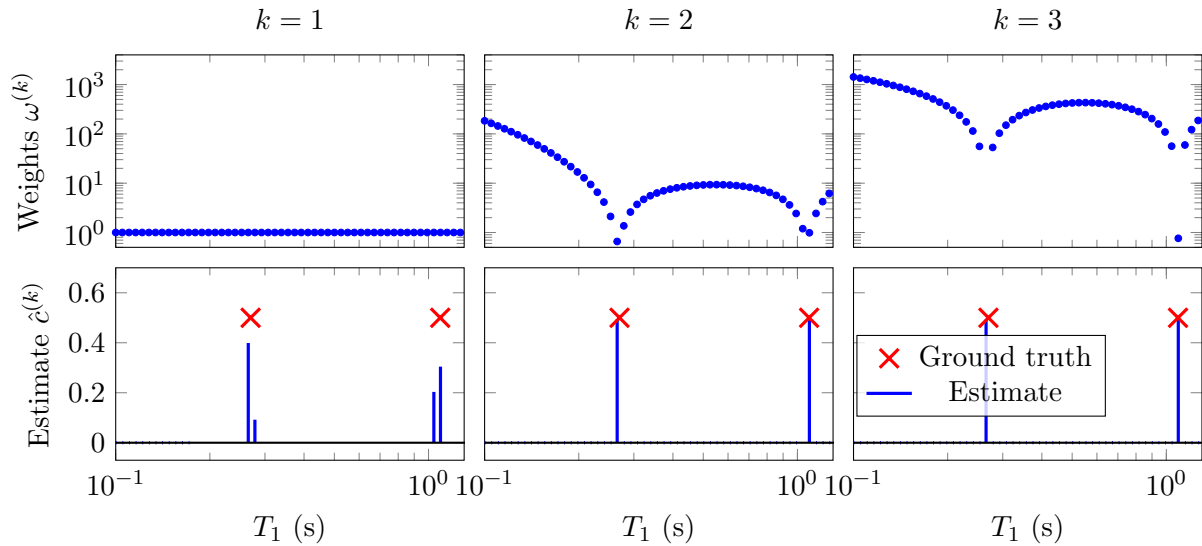


Figure 7: Solutions to problem (2.26) (bottom) and corresponding weights (top) computed following the reweighting scheme (2.28), with $\lambda := 10^{-3}$ and $\epsilon := 10^{-8}$. The data are the same as in Figure 5.

to be inversely proportional to the previous estimate $\hat{c}^{(k-1)}$

$$\omega_i^{(k)} := \frac{1}{\epsilon + |\hat{c}^{(k-1)}|}, \quad 1 \leq i \leq m, \quad (2.27)$$

where ϵ is a parameter typically fixed to a very small value with respect to the expected magnitude of the nonzero coefficients (e.g. 10^{-8}) in order to preclude division by zero. Intuitively, the weights penalize the coefficients that do not contribute to the fit in previous iterations, promoting increasingly sparse solutions. Mathematically, the algorithm can be interpreted as a majorization-minimization method for a non-convex sparsity-inducing penalty function [19]. The second updating scheme, proposed in [74] and inspired by sparse Bayesian learning methods [75], is of the form

$$\omega_i^{(k)} := \left(D_i^T (\epsilon I + DC^{-1}WD^T)^{-1} D_i \right)^{\frac{1}{2}}, \quad (2.28)$$

$$C := \text{diag} \left(\hat{c}^{(k-1)} \right), \quad (2.29)$$

$$W := \text{diag} \left(\omega^{(k-1)} \right), \quad (2.30)$$

where ϵ is a parameter which precludes the matrix $\epsilon I + DX^{-1}WD^T$ from being singular. The reweighting scheme sets $\omega_i^{(k)}$ to be small if there is any large entry $\hat{c}_j^{(k-1)}$ such that the corresponding columns of the dictionary D_i and D_j are correlated. This produces smoother weights than (2.27) providing more robustness to initial errors in the support estimate.

Figures 6 and 7 show the results obtained by applying reweighted- ℓ_1 -norm regularization to the same problem as in Figure 5. As expected, the update (2.28) yields smoother weights. Convergence to a sparse solution is achieved in just two iterations. The estimate is an accurate estimate of the parameters despite the presence of noise and the gridding error (the true parameters do not lie on the grid used to construct the dictionary).

In order to evaluate the performance of the sparse recovery algorithm, we carried out an experiment with data simulated from a voxel containing a 50%-50% mix of two compartments. The parameters of the first compartment are fixed ($T_1 = 0.21$ s, $T_2 = 9$ ms), whereas the parameters of the second compartment vary on a fine grid (T_1 between 0.1 s and 2.0 s and T_2 between 5 ms and 100 ms). The data were generated by adding the fingerprints from the two compartments and perturbing the result with i.i.d. Gaussian noise. Figure 8 shows the result of fitting the multicompartment model using the reweighting scheme defined in Eq. (2.28), as the parameters of the second compartment vary. In the noiseless case, exact recovery occurs (even without reweighting) except for very close values. For the noisy data, the algorithm tends to detect the correct number of components as long as the parameters of the two components are not too similar, i.e. they are sufficiently separated in parameter space (b, c). The accuracy of the parameter estimate then decreases as the noise level increases (e, f, h, i), resulting in some cases in the appearance of a spurious third compartment (b, c). When the parameters of both compartments are very close in parameter space, the algorithm tends to estimate a single compartment. This occurs in the red region around the green square in subfigure b. Increasing the noise increases the size of the region (c). Within it, one can observe that the reconstructed compartment lies between the two original compartments, as indicated by the slope in the error (e, f, h, i). Areas with $T_1 \approx T_2$ seem to be subject to a systematic overestimation of the number of compartments, as well as an overestimation of T_2 (c, i), while the error in the relaxation times is less structured in the rest of the parameter space (e, f, h, i).

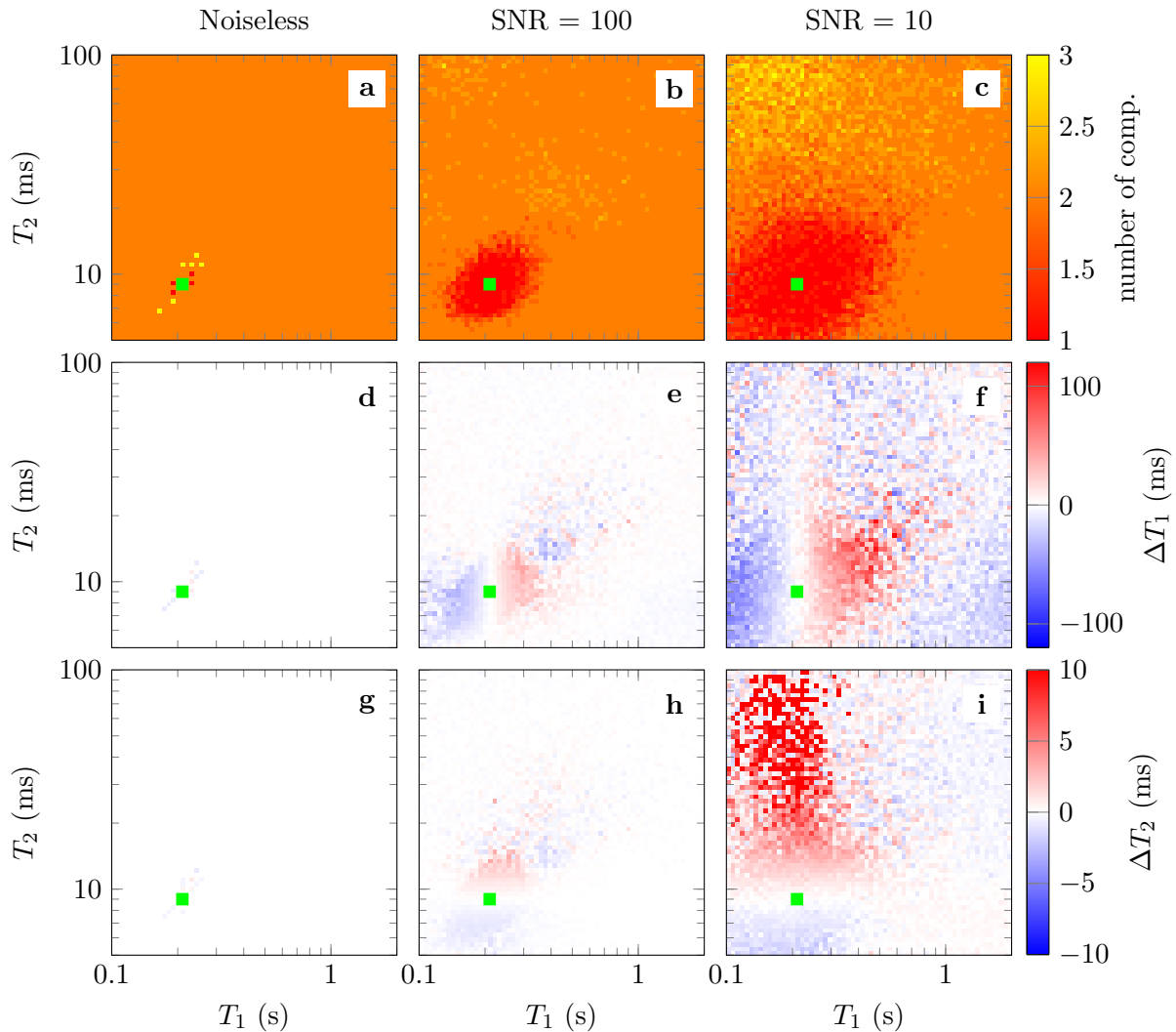


Figure 8: This figure depicts the results of reconstructing one compartment with $T_1 = 0.21$ s and $T_2 = 9$ ms (marked by the green square), in the presence of a second compartment with T_1 values between 0.1 s and 2.0 s and T_2 values between 5 ms and 100 ms (the proton density of each tissue is 0.5). The fingerprints were generated for a single-voxel without k-space undersampling and following Refs. [3, 4]. I.i.d. Gaussian noise is added to the simulated data. The reconstruction was performed with the reweighting scheme defined in Eq. (2.28), where the weighted ℓ_1 -norm minimization problems are solved using the method described in Section 2.6. The first row depicts the number of compartments resulting from the reconstruction (the ground truth is two). The second and third row show the T_1 and T_2 errors, respectively. These errors correspond to the signed distance between the relaxation times of the fixed compartment ($T_1 = 0.21$ s and $T_2 = 9$) and the closest relaxation time of the reconstructed atoms. The results are averaged over 5 repetitions with different noise realizations.

2.6 Fast interior-point solver for ℓ_1 -norm regularization in coherent dictionaries

In this section we describe an interior-point solver for the ℓ_1 -norm regularized problem

$$\begin{aligned} & \underset{\tilde{c} \in \mathbb{R}^m}{\text{minimize}} && \frac{1}{2} \|D\tilde{c} - x\|^2 + \lambda \sum_{i=1}^m \tilde{c}_i \\ & \text{subject to} && \tilde{c} \geq 0, \end{aligned} \quad (2.31)$$

which allows us to apply the reweighting schemes described in Section 2.5 efficiently. Interior-point methods enforce inequality constraints by using a barrier function [12, 58, 77]. In this case we use a logarithmic function that forces the coefficients to be nonnegative. Parametrizing the modified optimization problem with $t > 0$, we obtain a sequence of cost functions of the form

$$\phi_t(\tilde{c}) := \frac{1}{2} t \|D\tilde{c} - x\|^2 + t\lambda \sum_{i=1}^n \tilde{c}_i - \sum_{i=1}^n \log \tilde{c}_i. \quad (2.32)$$

The *central path* of the interior-point scheme consists of the minimizers of ϕ_t as t varies from 0 to ∞ . To find a solution for problem 2.31, we find a sequence of points $c^{(1)}, c^{(2)}, \dots$ in the central path by iteratively solving the Newton system

$$(Z + 2tD^T D) (c^{(k)} - c^{(k-1)}) = -\nabla \phi_t (c^{(k-1)}) \quad (2.33)$$

where

$$Z := \text{diag} \left(\frac{1}{\tilde{c}_1^2}, \dots, \frac{1}{\tilde{c}_m^2} \right). \quad (2.34)$$

This is essentially the approach taken in [13, 42] to tackle ℓ_1 -norm regularized least squares. Solving (2.33) is the computational bottleneck of this method. In the case of the MRF dictionary, $D^T D$ is a matrix of rank k , where k is the order of the low-rank approximation to the dictionary described in Section 2.3. As a result, solving the Newton system (2.33) directly is extremely slow for large values of t . Using a preconditioner of the form

$$P := 2t \text{diag}(D^T D) + Z \quad (2.35)$$

combined with an iterative conjugate-gradient method to invert the system, as suggested in [42], does not alleviate this problem due to the ill-conditioning of the matrix as t grows large.

In order to solve the Newton system (2.33) efficiently, we take a different route: exploiting the low-rank structure of the Hessian by applying the Woodbury inversion lemma, also known as Sherman-Morrison-Woodbury formula.

Lemma 2.1 (Woodbury inversion lemma). *Assume $A \in \mathbb{R}^{n \times n}$, $B, G \in \mathbb{R}^{n \times r}$ and $L \in \mathbb{R}^{r \times r}$. Then,*

$$(A + BLG^T)^{-1} = A^{-1} - A^{-1}B(L^{-1} + GA^{-1}B)^{-1}GA^{-1} \quad (2.36)$$

Setting $A := Z$, $B := D$, $G := D^T$ and $L := I \in \mathbb{R}^k$ in the lemma yields the following expression for the inverse of the system matrix

$$(Z + 2tD^T D)^{-1} = Z^{-1} - 2tZ^{-1}D^T(I^{-1} + 2tDZ^{-1}D^T)^{-1}DZ^{-1}. \quad (2.37)$$

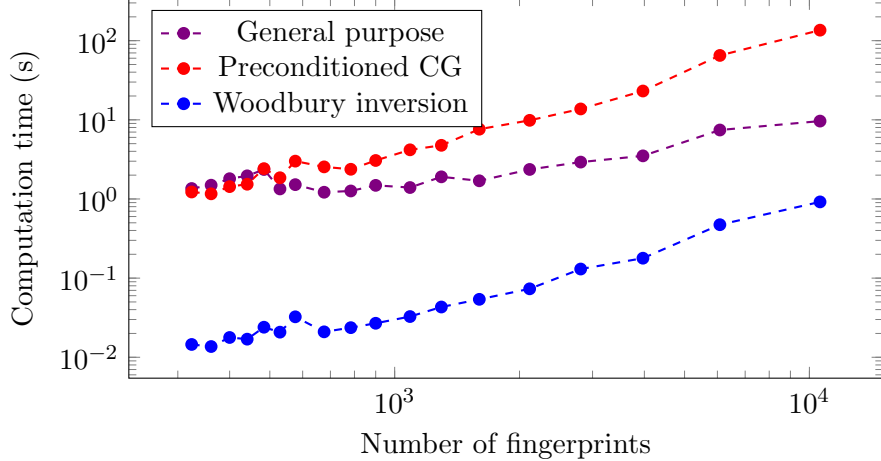


Figure 9: Computation times of the proposed Woodbury-inversion method compared to a general-purpose solver [35] and an approach based on preconditioned conjugate-gradients (CG) [42]. MRF dictionaries containing different numbers of fingerprints in the same range (T_1 values from 0.1 s to 2 s, T_2 values from 0.005 s to 0.1 s) were generated using the approach described in Refs. [3,4]. Each method was applied to solve 10 instances of problem (2.31) for each dictionary size on a computer cluster (Four AMD Opteron 6136, each with 32 cores, 2.4 GHz, 128 GB of RAM).

Since in practice k is very small (typically between 10 and 15) due to the dictionary-compression scheme described in Section 2.3 and Z is diagonal, using this formula accelerates the inversion of the Newton system dramatically.

Figure 9 compares the computational cost of our method based on Woodbury-inversion with a general-purpose convex-programming solver based on an interior-point method [35] and an interior-point method tailored to large-scale problems, which applies the preconditioner in Eq. (2.35) and uses an iterative method to solve the Newton system [42]. Our method is almost an order of magnitude faster for dictionaries containing up to 10^4 columns.

To conclude the section, we note that this algorithm can be directly applied to weighted ℓ_1 -norm-regularization least squares problems of the form

$$\begin{aligned}
 & \underset{\tilde{c} \in \mathbb{R}^m}{\text{minimize}} && \frac{1}{2} \|D\tilde{c} - x\|^2 + \lambda \sum_{i=1}^m W\tilde{c}_i \\
 & \text{subject to} && \tilde{c} \geq 0,
 \end{aligned} \tag{2.38}$$

where W is a diagonal matrix containing the weights. We just need to apply the change of variable $\tilde{c}' = W\tilde{c}$ and $D' = DW^{-1}$. Since the weights are all positive, the constraint $\tilde{c} \geq 0$ is equivalent to $\tilde{c}' \geq 0$.

3 Results

3.1 Simulations

In this section, we evaluate our methods on a numerical phantom that mimics an MRF experiment with radial k -space sampling. The numerical phantom has 16 different 19×19 voxel regions. The voxels in each region consist of either one or two compartments with relaxation times in the same range as biological tissues such as myelin water (A), gray matter (B), white matter (C), and cerebrospinal fluid (C). Figure 10 depicts the structure of the phantom along with the corresponding relaxation times. For each compartment, a fingerprint was calculated with Bloch simulations utilizing the flip angle pattern described in Fig. 3k in [4]. These fingerprints are then combined additively to yield the multicompartment fingerprints of each voxel. The data correspond to undersampled k -space data of each time frame, calculated with a non-uniform fast Fourier transform [2, 31] with 16 radial k -space spokes per time frame. The fingerprints consist of 850 time frames, and the trajectory of successive time frames are rotated by 16 times the golden angle with respect to each other [73]. Noise with an i.i.d Gaussian distribution was added to the simulated k -space data to achieve different signal-to-noise ratios.

When two different tissues are present in a voxel, two conditions are necessary so that the problem of distinguishing their contributions to the signal is well posed. First, their corresponding fingerprints should be sufficiently distinct, i.e. have a low correlation coefficient (c.f. Section 2.4). Second, the weighted sum of their fingerprints should be different from any other fingerprint in the dictionary. Otherwise, a single-compartment model will fit the data well. Figure 11 shows the correlations between the fingerprints corresponding to each of the tissues present in the numerical phantom and the rest of the fingerprints in the dictionary. For tissues that have similar T_1 and T_2 values, the correlation is very high. In particular, the fingerprints corresponding to tissue B and C are extremely similar. Furthermore, their additive combination is almost indistinguishable from another fingerprint also present in the dictionary, as illustrated in Figure 12. It will consequently be hardly possible to distinguish a voxel containing a single tissue with that particular fingerprint and a two-compartment voxel containing tissue B and C if there is even a very low level of noise in the data. For the other combinations of the four examined relaxation times, this is not the case.

To estimate the relaxation times T_1 and T_2 from the simulated data we apply the method described in Section 2.2 while fixing the number of ADMM iterations to 10. We compress the dictionary by truncating its SVD to obtain a rank-10 approximation, as described in Section 2.3. The magnetization vector \tilde{X} is updated by applying 10 conjugate-gradient iterations. The coefficient variable \tilde{C} is updated by applying the reweighted- ℓ_1 method described in Section 2.5 over 5 iterations with the reweighting scheme in equation (2.27) (the reweighting scheme (2.28) yields similar results).

Figure 13 shows the reconstructed parameter maps for an $SNR = 10^3$ (the SNR is defined by the ratio between the ℓ_2 -norm of the signal and the added noise), and using 16 radial k -space spokes. The multicompartment reconstruction recovers the two compartments accurately, except for the voxels that contain the highly correlated tissues B and C. This behavior is expected due to the high correlations of the fingerprints of those tissues (c.f. Figure 12). The model also yields an accurate estimate of the proton density of the compartments that are present in each voxel (except, again, for voxels containing tissue B and C). In most voxels, the reconstruction does not detect additional compartments, even though this is not explicitly enforced. Figure 14 shows that the performance

tissue	A	B	C	D
$T_1(s)$	0.21	0.66	0.91	2.32
$T_2(s)$	0.009	0.042	0.062	0.416

	Column 1	Column 2	Column 3	Column 4
Row 1	100% A	50% A + 50% B	50% A + 50% C	50% A + 50% D
Row 2	50% B + 50% A	100% B	50% B + 50% C	50% B + 50% D
Row 3	50% C + 50% A	50% C + 50% B	100% C	50% C + 50% D
Row 4	50% D + 50% A	50% D + 50% B	50% D + 50% C	100% D

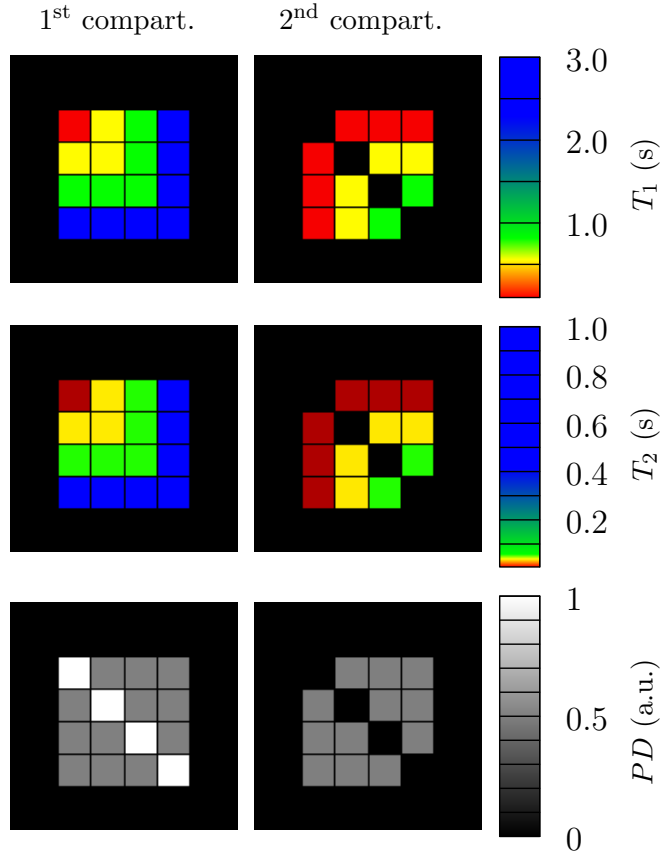


Figure 10: The numerical phantom consists of four different synthetic tissues with relaxation times in the range commonly found in biological brain tissue. In particular, the relaxation times of tissues A-D are in the range found in myelin water, gray matter, white matter, and cerebrospinal fluid. The phantom is a sum of rows and columns of the corresponding types of tissue in increasing order of the T_1 relaxation time. When sorting the compartments of each voxel by the T_1 relaxation time, the numerical phantom has the depicted diagonal structure.

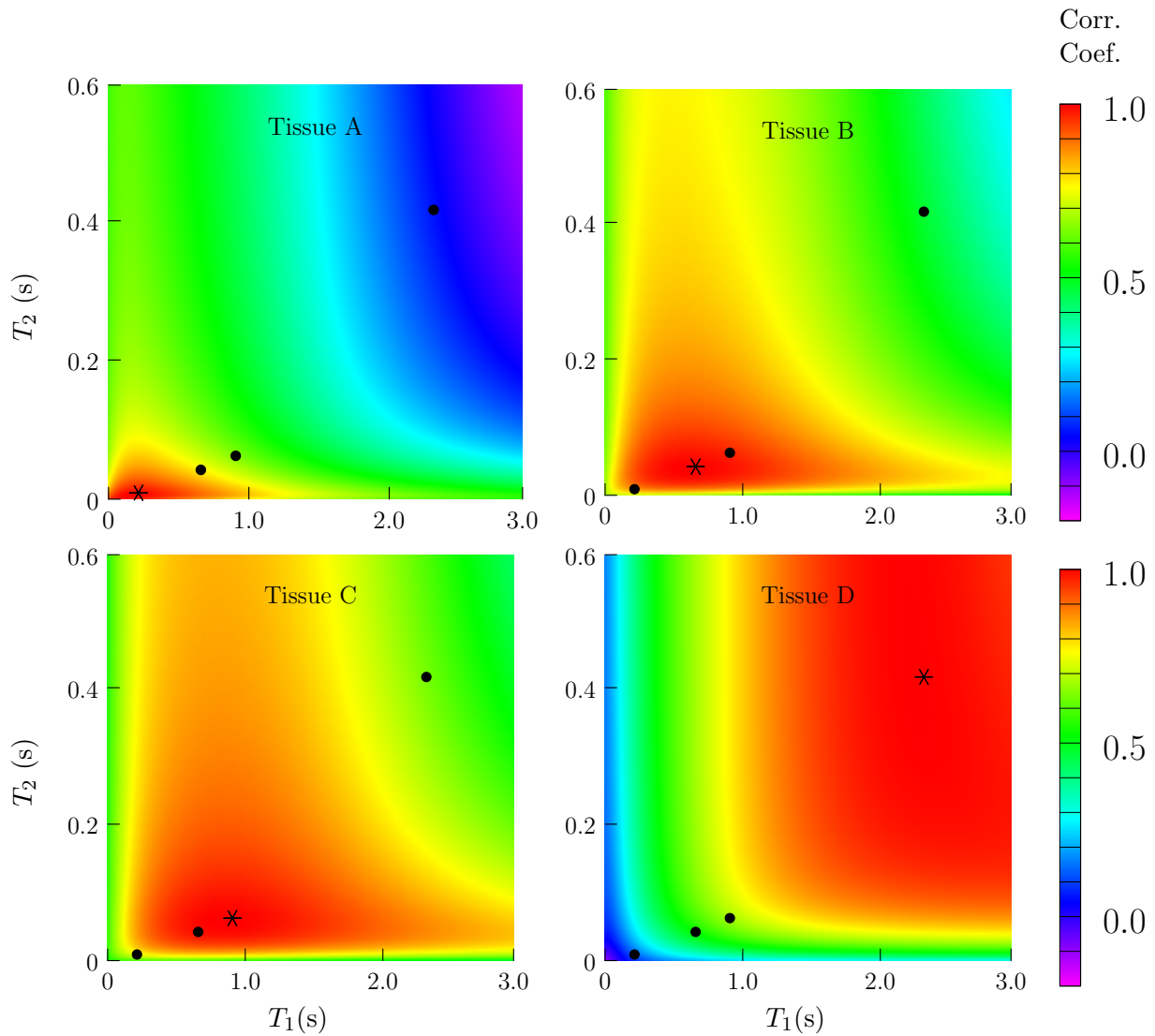


Figure 11: Correlation between the fingerprints corresponding to the four tissues with other fingerprints in the dictionary, indexed by their T_1 and T_2 values. The tissue corresponding to the fixed fingerprint is marked with a star, the position of the other three tissues also present in the phantom are marked with dots.

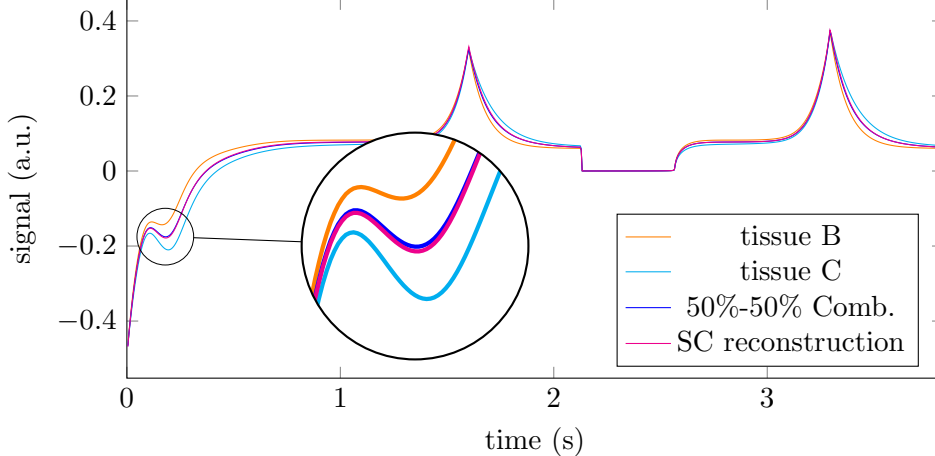


Figure 12: Simulated fingerprints of tissue B and C, and a 50%-50% combination of those tissues are shown, along with a single-compartment (SC) reconstruction, i.e. the fingerprint in the dictionary that is closest to the 50%-50% combination. In this particular example, the fingerprints of those tissues are highly correlated, and the single-compartment reconstruction represents the data well (the relative error in the ℓ_2 -norm is 1.42%). As a result, the multicompartement reconstruction cannot distinguish the two compartments if the data contain even a small level of noise.

degrades gracefully when the SNR is decreased to 100: the model still achieves similar results, only noisier, and a spurious third compartment with a relatively low proton density appears in some voxels.

To evaluate the performance of the method at different undersampling factors, we fit the multicompartement model to the simulated phantom data using different number of radial k-space spokes. Figure 15 shows the decrease in the normalized root-mean-square-error (NRMSE) of the T_1 and T_2 estimates averaged over all voxels in the phantom. As expected, the NRMSE decreases when acquiring more k-space spokes. As explained above, the largest contributor to the NRMSE are the voxels that contain both tissue B and C, so the NRMSE excluding these voxels is also depicted. The scatter plots in Figure 16 show the results at each voxel containing a 50%-50% mixture of tissue A and C. The two compartments are separated accurately, even when only two radial k-space spokes are measured. As more samples are gathered, the two clusters corresponding to the two tissues concentrate more tightly around the ground truth. Similarly, when keeping the number of k-space spokes fixed and increasing the SNR, the NRMSE decreases as expected (Figure 17) and the estimated parameters converge to the ground truth (Figure 18). The dependence of the reconstruction quality on the correlation of the fingerprints is visualized in Figure 19, where scatter plots for all tissue combinations are shown. One can observe a dependency of the reconstruction quality on the distance of the two compartments in parameter space. In particular, the combination of tissues B and C, which have highly correlated fingerprints, results in a single compartment fit (see Figure 12).

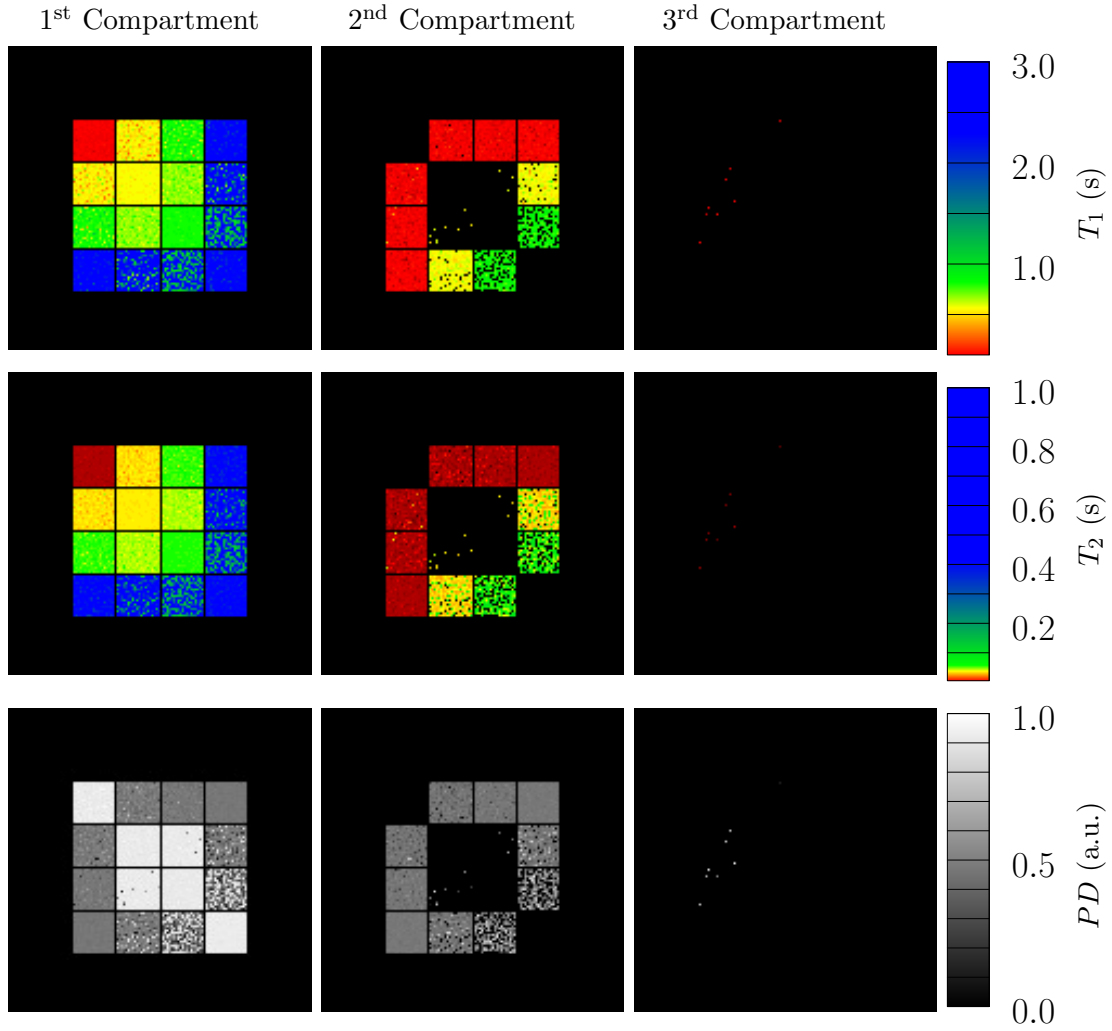


Figure 13: The depicted parameter maps were reconstructed from data simulated with an $\text{SNR} = 10^3$ and using 16 radial k-space spokes. The proton density (PD, third row) is here equivalent to the fraction of the recovered compartments. The compartments in each voxel are sorted according to their ℓ_2 -norm distance to the origin in T_1 - T_2 space. Compare to Figure 10, which shows the ground truth.

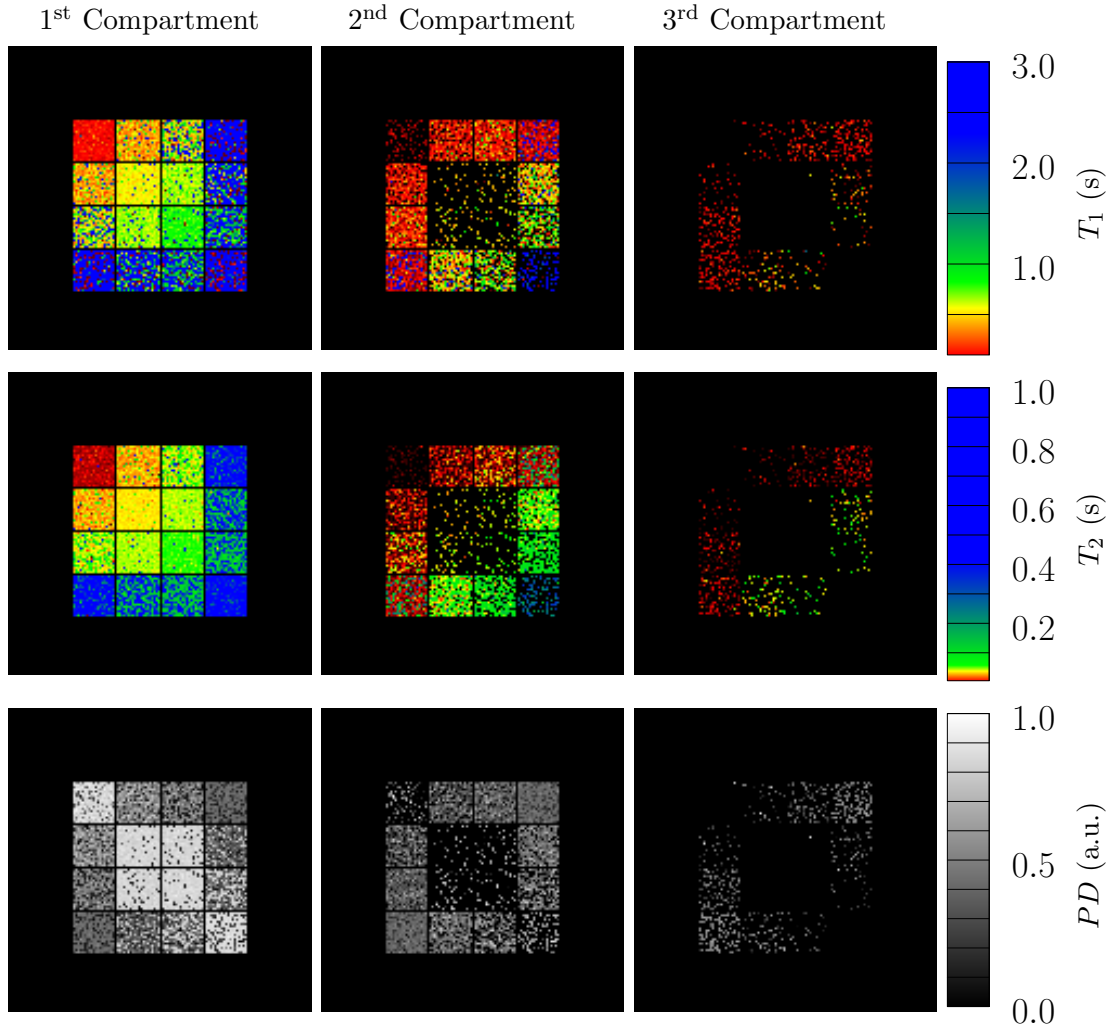


Figure 14: The depicted parameter maps were reconstructed from data simulated with an SNR = 100 and using 16 radial k-space spokes. The proton density (PD, third row) is here equivalent to the fraction of the recovered compartments. The compartments in each voxel are sorted according to their ℓ_2 -norm distance to the origin in T_1 - T_2 space. Compare to Figure 10, which shows the ground truth.

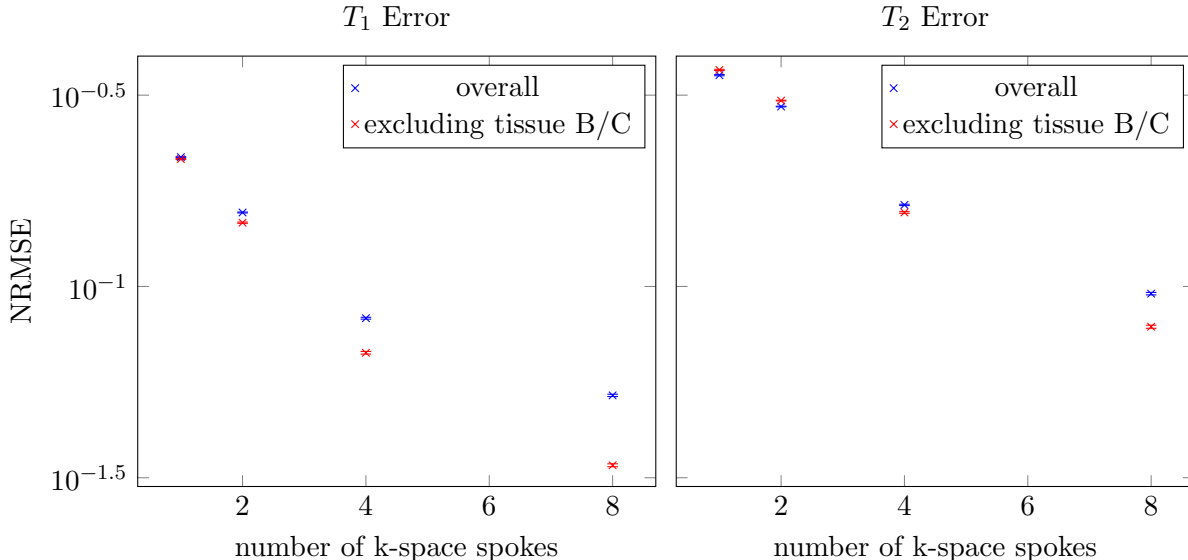


Figure 15: The normalized root-mean-square errors (NRMSE) in the T_1 and T_2 estimates are plotted as a function of the number of radial k-space spokes at a fixed SNR = 1000. The NRMSE is defined as the root-mean square of the $\Delta T_{1,2}/T_{1,2}$. The results are averaged over 10 realizations of the noise, and the hardly-visible error bars depict one standard deviation of the variation between different noise realizations. The NRMSE was also computed excluding voxels containing a combination of tissue B and C, because the corresponding fingerprints are highly correlated.

3.2 Phantom experiment

For validation on real data, we performed an imaging experiment on a clinical MR system with a field strength of 3 Tesla (Prisma, Siemens, Erlangen, Germany). We designed a dedicated phantom and manufactured it using a 3D printer (Figure 20). The structure of the phantom is effectively the same as that of the simulated phantom described in Section 3.1 and Figure 10: the diagonal elements contain only one compartment, whereas the off-diagonal elements contain two compartments. The compartments were filled with different solutions of doped water in order to achieve relaxation times in the range of biological tissues. MRF scans were performed with the sequence described in Fig. 3k of Ref. [4] with 8 radial k-space spokes per time frame and the same parameters otherwise.

Figure 21 shows the parameter maps reconstructed with a single-compartment model and a low-rank ADMM algorithm [2]. For the diagonal elements of the grid phantom, which only contain signal from a single compartment, we consider the identified T_1 and T_2 values listed in Table 1 as the reference gold standard. In the off-diagonal elements, the single-compartment model fails to account for the presence of two compartments, and the estimates are apparent relaxation times that lie in between the underlying values of the two compartments. Note that the square shape of the phantom causes significant variations in the main magnetic field towards the edges of the phantom. Since we do not account for those variations, substantial artifacts can be observed in those areas (Figure 21).

Figure 22 shows the parameter maps reconstructed with the proposed multicompartmen-

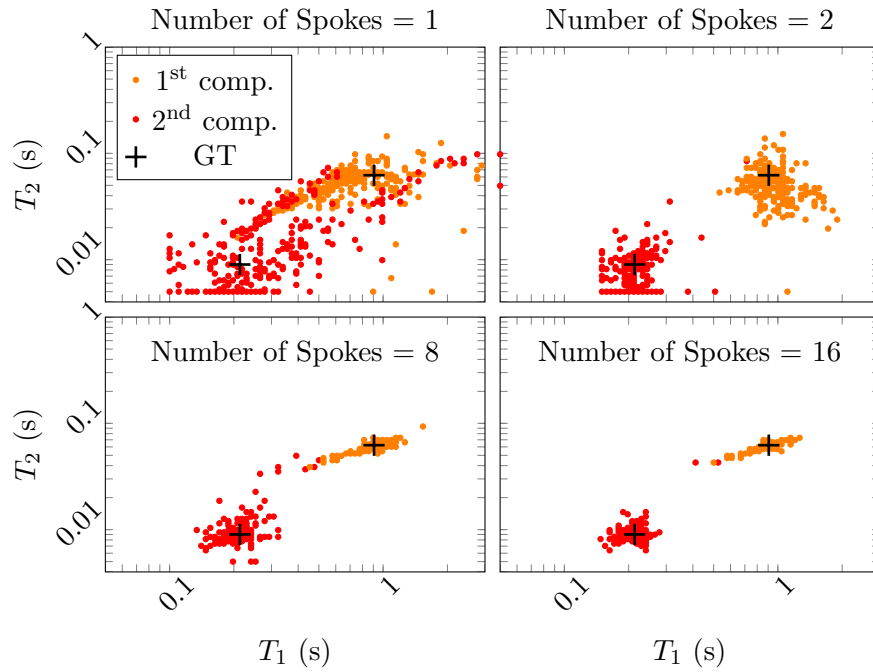


Figure 16: Scatter plots showing the estimated T_1 and T_2 values in the multicompartiment model for voxels containing tissue A and C. Different number of radial k-spaces spokes are tested at a fixed SNR of 10^3 . The two clusters corresponding to the two tissues concentrate more tightly around the ground truth (GT, marked with black crosses) as the number of spokes increases.

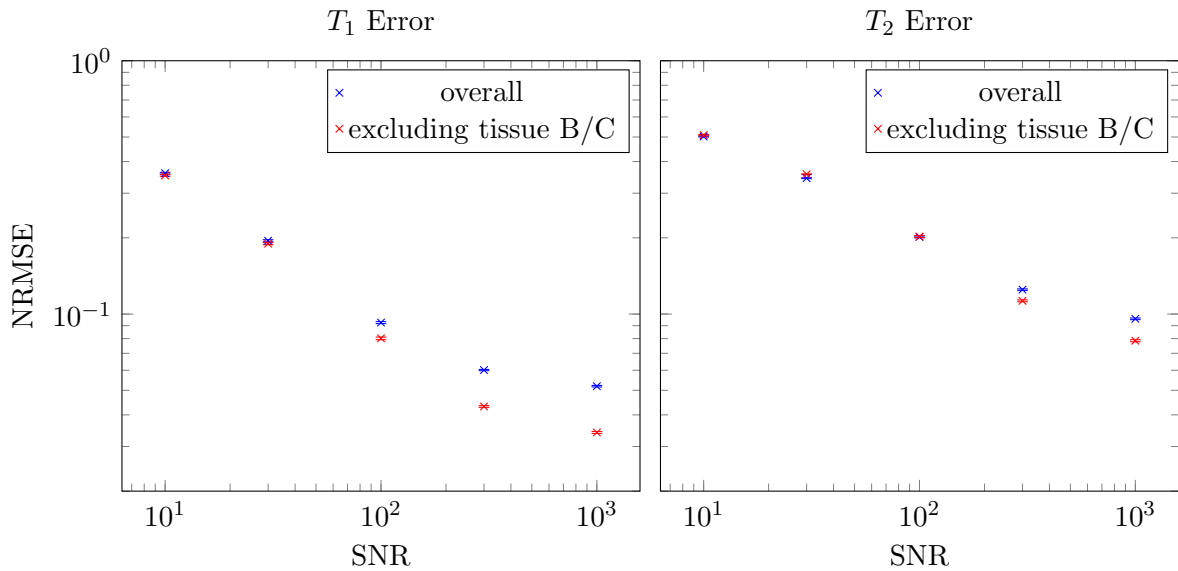


Figure 17: The normalized root-mean-square errors (NRMSE) in the T_1 and T_2 estimates are plotted as a function of the SNR when acquiring 8 radial k-space spokes. The NRMSE is defined as the root-mean square of the $\Delta T_{1,2}/T_{1,2}$. The results are averaged over 10 realizations of the noise, and the hardly-visible error bars depict one standard deviation of the variation between different noise realizations. The NRMSE was also computed excluding voxels containing a combination of tissue B and C, because the corresponding fingerprints are highly correlated.

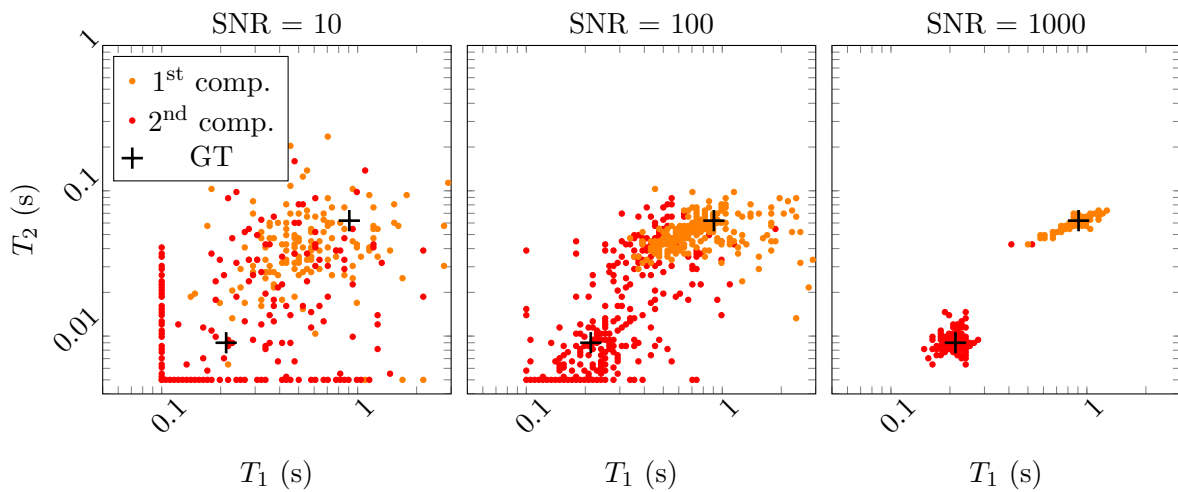


Figure 18: Scatter plots showing the estimated T_1 and T_2 values in the multicompartement model for voxels containing tissue A and C. The data was reconstructed from 16 radial k-space spokes. The two clusters corresponding to the two tissues concentrate more tightly around the ground truth (GT, marked with black crosses) as the SNR increases.

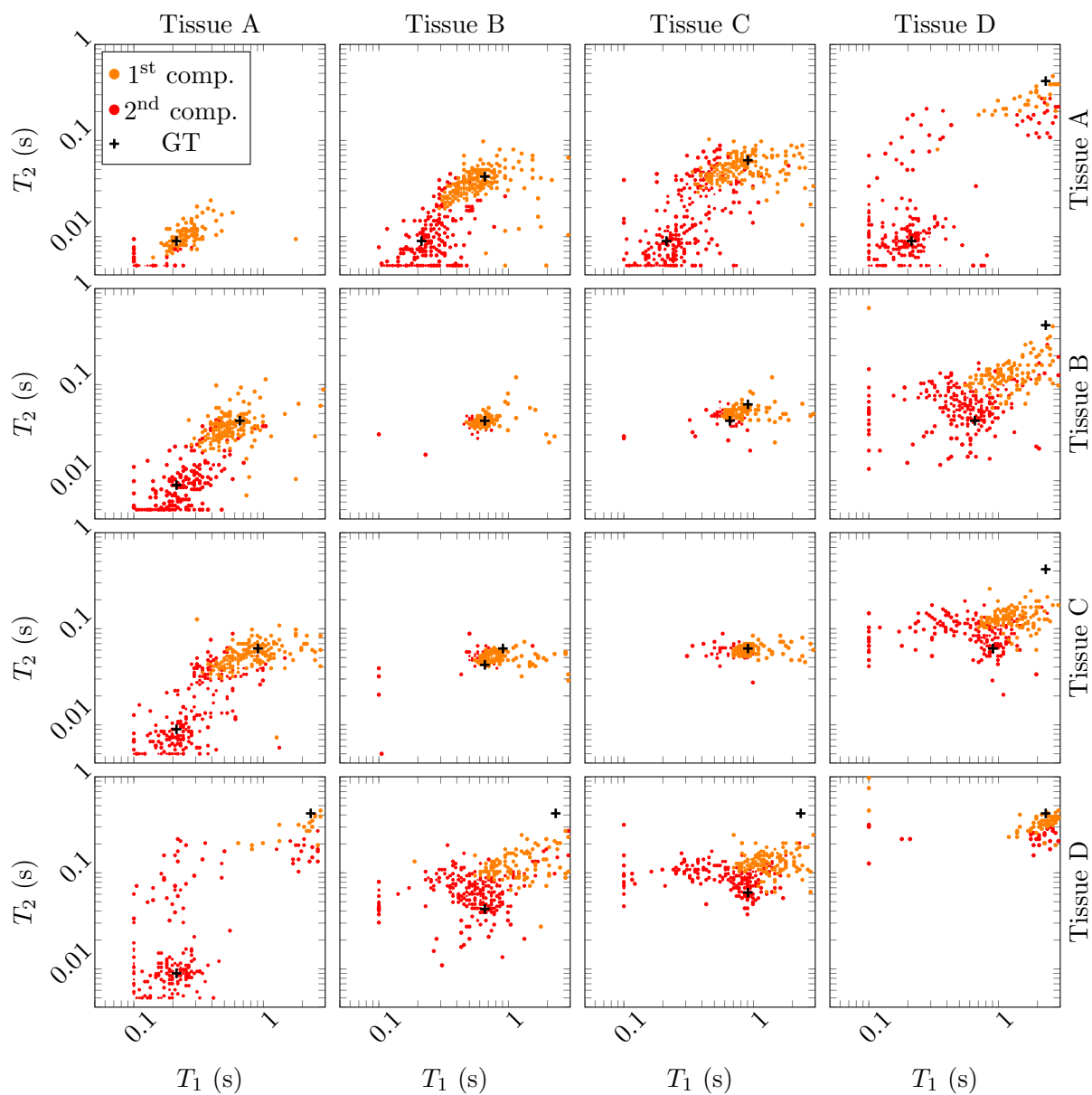


Figure 19: Scatter plots showing the estimated T_1 and T_2 values in the multicompartiment model for simulated data with an SNR = 100 and using 16 radial k-space spokes. Each subplot shows the estimated values of voxels containing combination of the tissue on the top and the tissue to the right of the subplot. The ground truth is also marked with black crosses as reference.

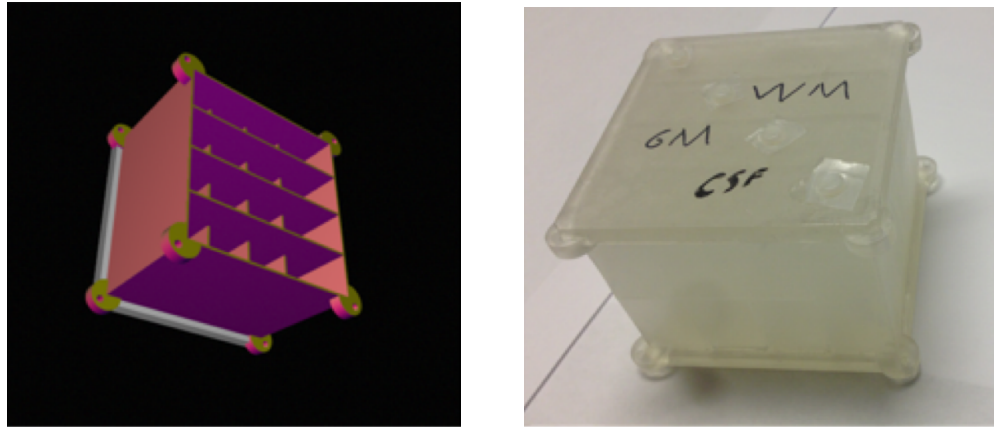


Figure 20: Computer-aided design (left) and the corresponding 3D-printed phantom (right) used for the phantom evaluation. It contains two layers, one with four horizontal and one with four vertical bars. Imaging a slice that contains both layers results in the same effective structure as the numerical phantom shown in Figure 10.

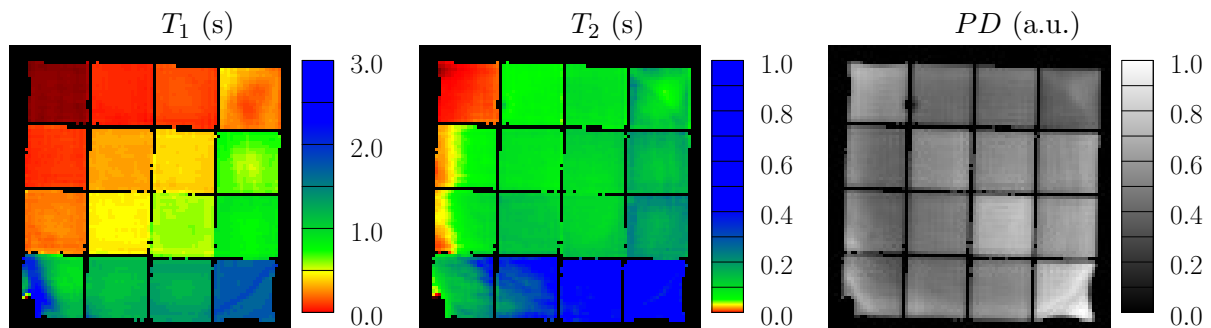


Figure 21: The depicted parameter maps were reconstructed from data measured in a phantom and using a single-compartment model. The data were acquired using 8 radial k-space spokes. The colorbar is adjusted so that distinct colors correspond to the parameters of the gold-standard reference measurements: red, yellow green and blue represent the solutions A-D.

	A	B	C	D
T_1 (s)	0.1262 ± 0.0075	0.5075 ± 0.015	0.7640 ± 0.055	1.831 ± 0.061
T_2 (s)	0.0174 ± 0.0046	0.1019 ± 0.0084	0.1328 ± 0.018	0.66 ± 0.21

Table 1: The gold-standard (GS) values measured by single-compartment reconstruction on the diagonal grids of phantom described in Figure 20, where only a single compartment is present.

	A and C		A and D		B and D	
	A	C	A	D	B	D
T_1 (s)	0.35 ± 0.25	0.58 ± 0.26	0.24 ± 0.26	1.40 ± 0.57	0.66 ± 0.18	1.49 ± 0.36
T_2 (s)	0.068 ± 0.071	0.20 ± 0.20	0.063 ± 0.24	1.20 ± 0.58	0.080 ± 0.11	1.25 ± 0.44

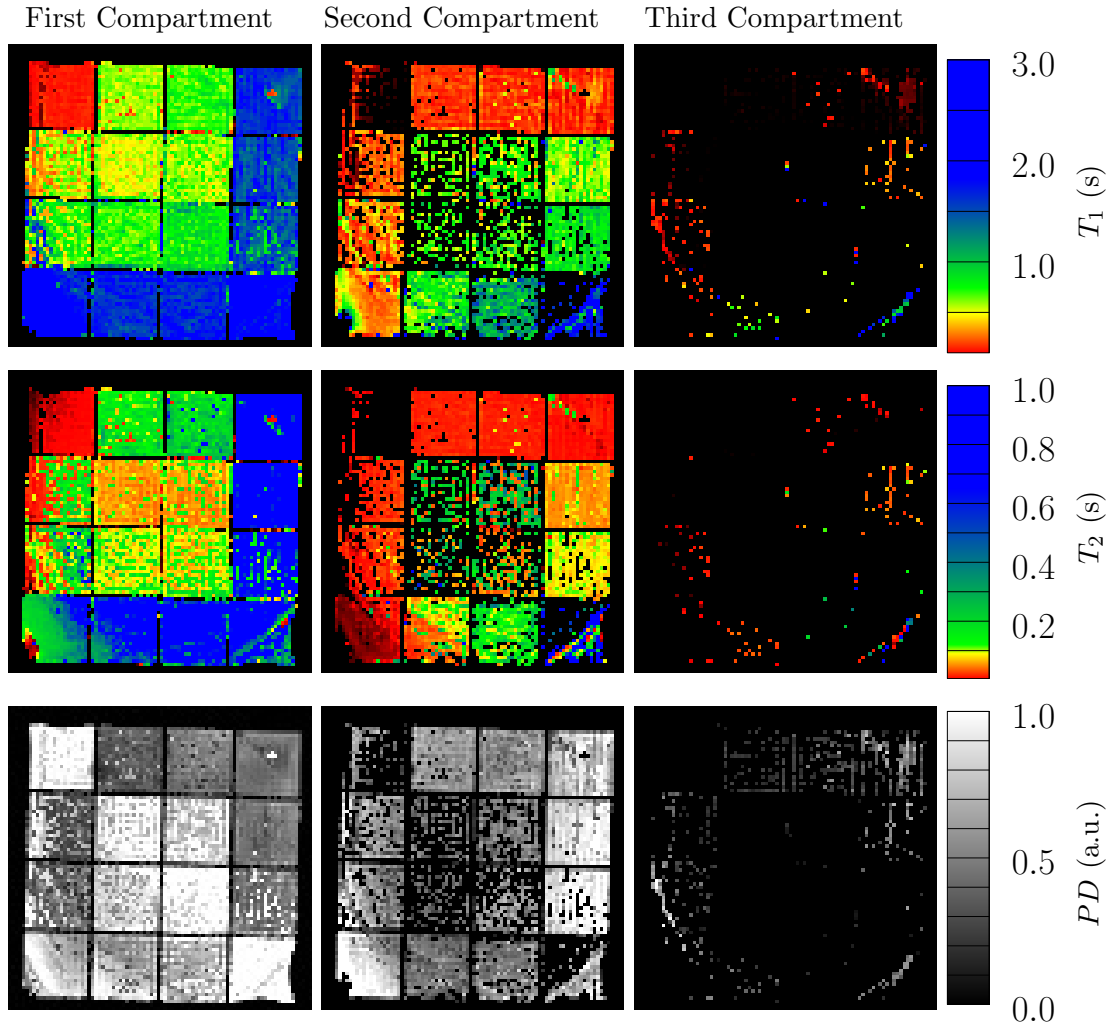
Table 2: Mean values and standard deviations of the multicompartment estimates for the selected combinations appearing in Figure 23.

reconstruction method. At the diagonal elements, results are consistent with the single-compartment reconstruction, except for some voxels where a spurious second compartment appears with low proton density. This indicates that the method correctly identifies voxels containing only a single compartment. In the off-diagonal grid elements, two significant compartments are detected for most voxels, and the relaxation times coincide with the gold-standard within a standard deviation (Table 2). However, the noise level is quite severe at the given experimental conditions. Further, a spurious third compartment with low proton density is detected in some voxels. In contrast, many voxels containing the combination of the doped water solutions B and C are reconstructed as a single compartment with apparent relaxation times between the gold-standard values. This is expected, since the corresponding fingerprints are almost indistinguishable, as in the case of the simulated tissues B and C (c.f. Fig. 8). Errors are larger for T_2 than for T_1 , as expected from the Cramér-Rao bound estimation performed in [4]. The artifacts towards the edge of the phantom are due to variations in the main magnetic field (c.f. to the single compartment reconstruction in Figure 21).

Further insights are provided by the scatter plots depicted in Figure 23, which combines the estimated relaxation times of all voxels containing respective combination of doped water solutions. The multicompartment reconstruction correctly detects the presence of both tissues and the estimated relaxation times cluster around the gold-standard values. In contrast, the single-compartment algorithm results in a single cluster of apparent relaxation times at a position in parameter space that provides little information about the underlying tissue composition.

4 Conclusions and Future Work

In this work we propose a framework to perform quantitative estimation of parameter maps from magnetic resonance fingerprinting data, which accounts for the presence of more than one tissue compartment in each voxel. This multi-compartment model is fitted to the data by solving a sparse linear inverse problem using reweighted ℓ_1 -norm regularization. Numerical simulations show that an efficient interior-point method is able to tackle this sparse-recovery problem, yielding sparse solutions that correspond to the parameters of the tissues present in the voxel. In contrast, alternative



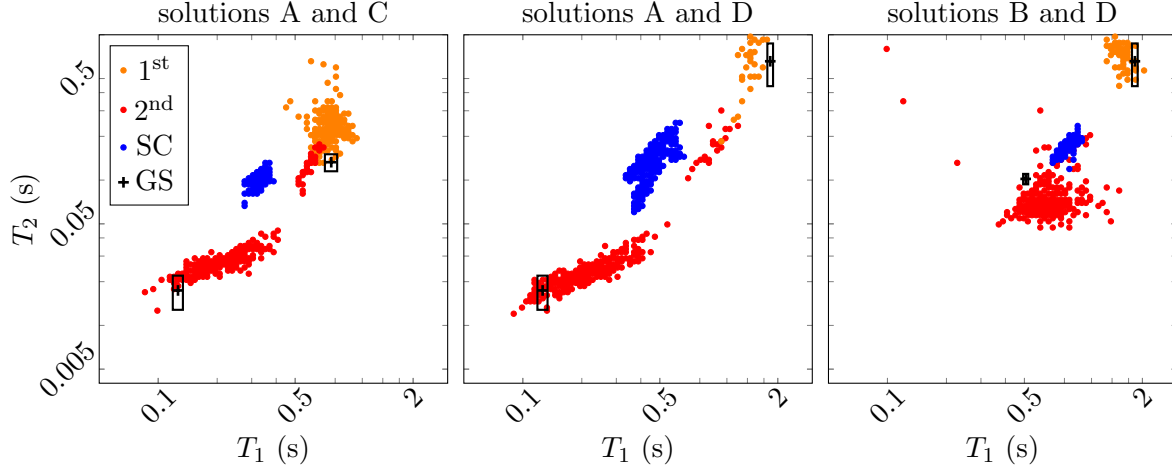


Figure 23: The scatter plot shows the estimated relaxation times of the measured phantom at the example of voxels containing different combinations of compartments. For comparison, the estimates obtained from the single-compartment (SC) are shown, as well as the gold-standard (GS) values measured on the diagonal, where only a single compartment is present. The rectangles represent the standard deviation of the gold-standard measurement.

approaches based on ℓ_2 -norm reweighting [54] yield locally dense solutions, which are interpreted as a probability density of the tissue parameters.

The proposed method is validated through simulations, as well as with a controlled phantom imaging experiment on a clinical MR system. The results indicate that incorporating a sparse-estimation procedure based on reweighted ℓ_1 -norm regularization is a promising avenue towards achieving multicompartment parameter mapping from MRF data. However, the proposed method still requires a high SNR, which entails long scan times for in vivo applications. A promising research direction is to incorporate additional prior assumptions on the structure of the parameter maps in order to leverage the method in the realm of clinically-feasible scan times. Future work will further include the application of the proposed framework to the quantification of the myelin-water fraction in the human brain, which is an important biomarker for neurodegenerative disease.

Acknowledgements

C.F. is supported by NSF award DMS-1616340. J.A., F.K., R.L. and M.C. are supported by NIH/NIBIB R21 EB020096, NIH/NIAMS R01 AR070297 and NIH P41 EB017183. S. L. is supported by a seed grant from the Moore-Sloan Data-Science Environment at NYU. S. T. is supported in part by the Office of Naval Research under Award N00014-17-1-2059.

References

- [1] A. Allerhand and H. S. Gutowsky. Spin-Echo NMR Studies of Chemical Exchange. I. Some General Aspects. *The Journal of Chemical Physics*, 41:2115–2126, Oct. 1964.
- [2] J. Assländer, M. A. Cloos, F. Knoll, D. K. Sodickson, J. Hennig, and R. Lattanzi. Low rank alternating direction method of multipliers reconstruction for mr fingerprinting. *Magnetic Resonance in Medicine*, 79(1):83–96, 2018.
- [3] J. Assländer, S. J. Glaser, and J. Hennig. Pseudo steady-state free precession for mr-fingerprinting. *Magnetic resonance in medicine*, 77(3):1151–1161, 2017.
- [4] J. Assländer, R. Lattanzi, D. K. Sodickson, and M. A. Cloos. Relaxation in Spherical Coordinates: Analysis and Optimization of pseudo-SSFP based MR-Fingerprinting. *arXiv*, 1703.00481(v1), 2017.
- [5] A. Beck and M. Teboulle. A fast iterative shrinkage-thresholding algorithm for linear inverse problems. *SIAM journal on imaging sciences*, 2(1):183–202, 2009.
- [6] S. R. Becker, E. J. Candès, and M. C. Grant. Templates for convex cone problems with applications to sparse signal recovery. *Mathematical programming computation*, 3(3):165–218, 2011.
- [7] B. Bernstein and C. Fernandez-Granda. Deconvolution of Point Sources: A Sampling Theorem and Robustness Guarantees. *preprint*, 2017.
- [8] P. J. Bickel, Y. Ritov, and A. B. Tsybakov. Simultaneous analysis of lasso and $\{D\}$ antzig selector. *The Annals of Statistics*, pages 1705–1732, 2009.
- [9] F. Bloch. Nuclear induction. *Physical review*, 70(7-8):460, 1946.
- [10] T. Blumensath and M. E. Davies. Iterative hard thresholding for compressed sensing. *Applied and computational harmonic analysis*, 27(3):265–274, 2009.
- [11] S. Boyd, N. Parikh, E. Chu, B. Peleato, and J. Eckstein. Distributed optimization and statistical learning via the alternating direction method of multipliers. *Foundations and Trends® in Machine Learning*, 3(1):1–122, 2011.
- [12] S. Boyd and L. Vandenberghe. *Convex optimization*. Cambridge university press, 2004.
- [13] E. Candes and J. Romberg. l1-magic: Recovery of sparse signals via convex programming. *URL: www.acm.caltech.edu/l1magic/downloads/l1magic.pdf*, 4:14, 2005.
- [14] E. J. Candes. The restricted isometry property and its implications for compressed sensing. *Comptes Rendus Mathematique*, 346(9-10):589–592, 2008.
- [15] E. J. Candès and C. Fernandez-Granda. Towards a Mathematical Theory of Super-resolution. *Communications on Pure and Applied Mathematics*, 67(6):906–956, 2014.
- [16] E. J. Candès, J. Romberg, and T. Tao. Robust uncertainty principles: Exact signal reconstruction from highly incomplete frequency information. *IEEE Transactions on information theory*, 52(2):489–509, 2006.
- [17] E. J. Candes and T. Tao. Decoding by linear programming. *IEEE transactions on information theory*, 51(12):4203–4215, 2005.
- [18] E. J. Candes and T. Tao. Near-optimal signal recovery from random projections: Universal encoding strategies? *IEEE transactions on information theory*, 52(12):5406–5425, 2006.
- [19] E. J. Candes, M. B. Wakin, and S. P. Boyd. Enhancing sparsity by reweighted l1 minimization. *Journal of Fourier analysis and applications*, 14(5):877–905, 2008.
- [20] S. S. Chen, D. L. Donoho, and M. A. Saunders. Atomic decomposition by basis pursuit. *SIAM review*, 43(1):129–159, 2001.

- [21] M. A. Cloos, F. Knoll, T. Zhao, K. Block, M. Bruno, C. Wiggins, and D. K. D. Sodickson. Multiparametric imaging with heterogenous radiofrequency fields. *Nature Communication*, 7:doi:10.1038/ncomms12445, nov 2016.
- [22] P. L. Combettes and V. R. Wajs. Signal recovery by proximal forward-backward splitting. *Multiscale Modeling & Simulation*, 4(4):1168–1200, 2005.
- [23] S. C. Deoni. Quantitative Relaxometry of the Brain. *Topics in Magnetic Resonance Imaging*, 21(2):101–113, 2010.
- [24] S. C. L. Deoni, L. Matthews, and S. H. Kolind. One component? two components? three? the effect of including a nonexchanging free water component in multicomponent driven equilibrium single pulse observation of t1 and t2. *Magnetic Resonance in Medicine*, 70(1):147–154, 2013.
- [25] S. C. L. Deoni, B. K. Rutt, T. Arun, C. Pierpaoli, and D. K. Jones. Gleaning multicomponent T1 and T2 information from steady-state imaging data. *Magnetic Resonance in Medicine*, 60(6):1372–1387, 2008.
- [26] A. Deshmane, D. McGivney, C. Badve, A. Yu, Y. Jiang, D. Ma, and M. A. Griswold. Accurate synthetic FLAIR images using partial volume corrected MR fingerprinting. In *Proceedings of the 24th Annual Meeting of ISMRM*, page 1909, 2016.
- [27] D. L. Donoho. Compressed sensing. *IEEE Transactions on information theory*, 52(4):1289–1306, 2006.
- [28] D. L. Donoho and M. Elad. Optimally sparse representation in general (nonorthogonal) dictionaries via l1 minimization. *Proceedings of the National Academy of Sciences*, 100(5):2197–2202, 2003.
- [29] E. Esser, Y. Lou, and J. Xin. A method for finding structured sparse solutions to nonnegative least squares problems with applications. *SIAM Journal on Imaging Sciences*, 6(4):2010–2046, 2013.
- [30] C. Fernandez-Granda. Super-resolution of point sources via convex programming. *Information and Inference*, 5(3):251–303, 2016.
- [31] J. Fessler and B. Sutton. Nonuniform fast fourier transforms using min-max interpolation. *IEEE Trans. Signal Process.*, 51(2):560–574, feb 2003.
- [32] J. Friedman, T. Hastie, and R. Tibshirani. *The elements of statistical learning*, volume 1. Springer series in statistics Springer, Berlin, 2001.
- [33] J. Friedman, T. Hastie, and R. Tibshirani. Regularization paths for generalized linear models via coordinate descent. *Journal of statistical software*, 33(1):1, 2010.
- [34] J. N. Giedd, J. W. Snell, N. Lange, J. C. Rajapakse, B. J. Casey, P. L. Kozuch, A. C. Vaituzis, Y. C. Vauss, S. D. Hamburger, D. Kaysen, and Others. Quantitative magnetic resonance imaging of human brain development: ages 4–18. *Cerebral cortex*, 6(4):551–559, 1996.
- [35] M. Grant, S. Boyd, M. Grant, S. Boyd, V. Blondel, S. Boyd, and H. Kimura. Cvx: Matlab software for disciplined convex programming, version 2.1. *Recent Advances in Learning and Control*, pages 95–110.
- [36] R. Gribonval and M. Nielsen. Sparse representations in unions of bases. *IEEE transactions on Information theory*, 49(12):3320–3325, 2003.
- [37] R. N. Gunn, S. R. Gunn, F. E. Turkheimer, J. A. Aston, and V. J. Cunningham. Positron emission tomography compartmental models: a basis pursuit strategy for kinetic modeling. *Journal of Cerebral Blood Flow & Metabolism*, 22(12):1425–1439, 2002.
- [38] J. I. Hamilton, A. Deshmane, S. Hougen, M. Griswold, and N. Seiberlich. Magnetic Resonance Fingerprinting with Chemical Exchange (MRF-X) for Quantification of Subvoxel T1, T2, Volume Fraction, and Exchange Rate. In *Proc. Intl. Soc. Mag. Reson. Med. 23*, page 329, 2015.

- [39] X. Han, J. Jovicich, D. Salat, A. van der Kouwe, B. Quinn, S. Czanner, E. Busa, J. Pacheco, M. Albert, R. Killiany, P. Maguire, D. Rosas, N. Makris, A. Dale, B. Dickerson, and B. Fischl. Reliability of MRI-derived measurements of human cerebral cortical thickness: The effects of field strength, scanner upgrade and manufacturer. *NeuroImage*, 32(1):180–194, 2006.
- [40] T. Hastie, R. Tibshirani, and M. Wainwright. *Statistical learning with sparsity*. CRC press, 2015.
- [41] P. Heins, M. Moeller, and M. Burger. Locally sparse reconstruction using the $\ell_{1,\infty}$ -norm. *arXiv preprint arXiv:1405.5908*, 2014.
- [42] S.-J. Kim, K. Koh, M. Lustig, S. Boyd, and D. Gorinevsky. An interior-point method for large-scale ℓ_1 -regularized least squares. *IEEE journal of selected topics in signal processing*, 1(4):606–617, 2007.
- [43] C. Laule, E. Leung, D. K. Li, A. L. Traboulsee, D. W. Paty, A. L. MacKay, and G. R. Moore. Myelin water imaging in multiple sclerosis: quantitative correlations with histopathology. *Multiple Sclerosis Journal*, 12(6):747–753, 2006.
- [44] C. Laule, I. M. Vavasour, G. R. W. Moore, J. Oger, D. K. B. Li, D. W. Paty, and A. L. MacKay. Water content and myelin water fraction in multiple sclerosis: A T2 relaxation study. *Journal of Neurology*, 251(3):284–293, 2004.
- [45] Z.-P. Liang and P. C. Lauterbur. *Principles of magnetic resonance imaging: a signal processing perspective*. The Institute of Electrical and Electronics Engineers Press, 2000.
- [46] S. Ljunggren. A simple graphical representation of Fourier-based imaging methods. *Journal of Magnetic Resonance (1969)*, 54(2):338–343, 1983.
- [47] M. Lustig, D. L. Donoho, J. M. Santos, and J. M. Pauly. Compressed Sensing {MRI}. *IEEE Signal Processing Magazine*, 25(2):72–82, mar 2008.
- [48] D. Ma, V. Gulani, N. Seiberlich, K. Liu, J. L. Sunshine, J. L. Duerk, and M. A. Griswold. Magnetic resonance fingerprinting. *Nature*, 495(7440):187–192, mar 2013.
- [49] J. Mairal, F. Bach, and J. Ponce. Sparse modeling for image and vision processing. *Foundations and Trends® in Computer Graphics and Vision*, 8(2-3):85–283, 2014.
- [50] D. Malioutov, M. Çetin, and A. S. Willsky. A sparse signal reconstruction perspective for source localization with sensor arrays. *IEEE transactions on signal processing*, 53(8):3010–3022, 2005.
- [51] S. Mallat. *A wavelet tour of signal processing: the sparse way*. Academic press, 2008.
- [52] S. G. Mallat and Z. Zhang. Matching pursuits with time-frequency dictionaries. *IEEE Transactions on signal processing*, 41(12):3397–3415, 1993.
- [53] S. J. Matzat, J. van Tiel, G. E. Gold, and E. H. Oei. Quantitative MRI techniques of cartilage composition. *Quantitative imaging in medicine and surgery*, 3(3):162, 2013.
- [54] D. McGivney, A. Deshmane, Y. Jiang, D. Ma, C. Badve, A. Sloan, V. Gulani, and M. Griswold. Bayesian estimation of multicomponent relaxation parameters in magnetic resonance fingerprinting. *Magnetic Resonance in Medicine*, 2017.
- [55] D. Needell and J. A. Tropp. CoSaMP: Iterative signal recovery from incomplete and inaccurate samples. *Applied and Computational Harmonic Analysis*, 26(3):301–321, 2009.
- [56] M. Neema, J. Stankiewicz, A. Arora, V. S. Dandamudi, C. E. Batt, Z. D. Guss, A. Al-Sabbagh, and R. Bakshi. T1-and T2-based MRI measures of diffuse gray matter and white matter damage in patients with multiple sclerosis. *Journal of Neuroimaging*, 17(s1), 2007.
- [57] D. G. Nishimura. *Principles of magnetic resonance imaging*. Stanford University, 1996.
- [58] J. Nocedal and S. Wright. *Numerical optimization*. Springer, 2006.

- [59] U. Nöth, E. Hattingen, O. Bähr, J. Tichy, and R. Deichmann. Improved visibility of brain tumors in synthetic MP-RAGE anatomies with pure T1 weighting. *NMR in Biomedicine*, 28(7):818–830, 2015.
- [60] Y. C. Pati, R. Rezaifar, and P. S. Krishnaprasad. Orthogonal matching pursuit: Recursive function approximation with applications to wavelet decomposition. In *Twenty-Seventh Asilomar Conference on Signals, Systems and Computers*, pages 40–44. IEEE, 1993.
- [61] L. C. Potter, E. Ertin, J. T. Parker, and M. Cetin. Sparsity and compressed sensing in radar imaging. *Proceedings of the IEEE*, 98(6):1006–1020, 2010.
- [62] K. P. Pruessmann, M. Weiger, M. B. Scheidegger, and P. Boesiger. SENSE: Sensitivity encoding for fast MRI. *Magnetic Resonance in Medicine*, 42(5):952–962, 1999.
- [63] D. S. Reich, S. A. Smith, K. M. Zackowski, E. M. Gordon-Lipkin, C. K. Jones, J. A. Farrell, S. Mori, P. C. van Zijl, and P. A. Calabresi. Multiparametric magnetic resonance imaging analysis of the corticospinal tract in multiple sclerosis. *Neuroimage*, 38(2):271–279, 2007.
- [64] J. R. Shewchuk. An Introduction to the Conjugate Gradient Method Without the Agonizing Pain. 1994.
- [65] C. Silva, J. Maltez, E. Trindade, A. Arriaga, and E. Ducla-Soares. Evaluation of l1 and l2 minimum norm performances on EEG localizations. *Clinical neurophysiology*, 115(7):1657–1668, 2004.
- [66] D. K. Sodickson and W. J. Manning. Simultaneous Acquisition of Spatial Harmonics (SMASH): Fast Imaging with Radiofrequency Coil Arrays. *Magnetic Resonance in Medicine*, 38(4):591–603, 1997.
- [67] R. L. Suddath, M. F. Casanova, T. E. Goldberg, D. G. Daniel, J. R. Kelsoe, D. R. Weinberger, and Others. Temporal lobe pathology in schizophrenia: a quantitative magnetic resonance imaging study. *Am J Psychiatry*, 146(4):464–472, 1989.
- [68] R. Tibshirani. Regression shrinkage and selection via the lasso. *Journal of the Royal Statistical Society. Series B (Methodological)*, pages 267–288, 1996.
- [69] P. Tofts. *Quantitative MRI of the brain: measuring changes caused by disease*. John Wiley & Sons, 2005.
- [70] J. Tohka. Partial volume effect modeling for segmentation and tissue classification of brain magnetic resonance images: A review. *World journal of radiology*, 6(11):855, 2014.
- [71] J. A. Tropp. Greed is good: Algorithmic results for sparse approximation. *IEEE Transactions on Information theory*, 50(10):2231–2242, 2004.
- [72] D. B. Twieg. The k-trajectory formulation of the NMR imaging process with applications in analysis and synthesis of imaging methods. *Medical Physics*, 10(5):610–621, 1983.
- [73] S. Winkelmann, T. Schaeffter, T. Koehler, H. Eggers, and O. Doessel. An optimal radial profile order based on the golden ratio for time-resolved MRI. *IEEE Transactions on Medical Imaging*, 26(1):68–76, 2007.
- [74] D. Wipf and S. Nagarajan. Iterative reweighted ℓ_1 and ℓ_2 methods for finding sparse solutions. *IEEE Journal of Selected Topics in Signal Processing*, 4(2):317–329, 2010.
- [75] D. P. Wipf and B. D. Rao. Sparse Bayesian learning for basis selection. *IEEE Transactions on Signal processing*, 52(8):2153–2164, 2004.
- [76] J. Wright, Y. Ma, J. Mairal, G. Sapiro, T. S. Huang, and S. Yan. Sparse representation for computer vision and pattern recognition. *Proceedings of the IEEE*, 98(6):1031–1044, 2010.
- [77] S. J. Wright. *Primal-dual interior-point methods*. SIAM, 1997.
- [78] P. Xu, Y. Tian, H. Chen, and D. Yao. Lp norm iterative sparse solution for EEG source localization. *IEEE transactions on biomedical engineering*, 54(3):400–409, 2007.